

Unravelling complex geologic histories using U–Pb and trace element systematics of titanite

Hugo K. H. Olierook^{1†*}, Richard J. M. Taylor^{1,2}, Timmons M. Erickson^{1,3}, Chris Clark¹, Steven M. Reddy¹, Christopher L. Kirkland^{1,4}, Inalee Jahn¹, Milo Barham¹

¹School of Earth and Planetary Sciences, Curtin University, GPO Box U1987, Perth, WA 6845, Australia

²Department of Earth Sciences, University of Cambridge, Cambridge CB2 3EQ, UK

³Center for Lunar and Space Exploration, Lunar and Planetary Institute – Universities Space Research Association, 3600 Bay Area Boulevard, Houston, TX, 77058, USA

⁴Centre for Exploration Targeting – Curtin Node; School of Earth and Planetary Sciences, Curtin University, GPO Box U1987, Perth, WA 6845, Australia

*Corresponding author: hugo.olierook@curtin.edu.au

Keywords: Spheene; Zircon; Gascoyne; Mutherbukin; geochronology; petrochronology

Abstract

Unravelling the spatio-temporal evolution of orogenic terranes requires a comprehensive understanding of the duration and extent of metamorphic events and hydrothermal alteration. Commonly used minerals such as zircon and monazite may not fully record geological histories in complex tectonic settings because their elemental constituents do not react under many metamorphic and metasomatic conditions. Here, we complement the current geochronological record of the Capricorn Orogen, Western Australia, with titanite U–Pb geochronology and geochemistry of felsic intrusive rocks to draw conclusions about the use of titanite in understanding the evolution of orogenic terranes. Because titanite usually incorporates common-Pb and may be variably reset by multiple metamorphic and hydrothermal events, a workflow is provided here for the systematic and robust interpretation of titanite U–Pb data. The addition of trace element data in titanite is particularly effective for differentiating whether a grain is igneous, recrystallized or metamorphic. We have developed several petrogenetic indices to differentiate these three types of titanite using Zr-in-titanite temperature, Th/U, Th/Pb, Al/(Al+Fe), light to heavy rare earth element ratio, and Eu anomalies. The addition of trace element geochemistry can also highlight anomalously radiogenic $^{207}\text{Pb}/^{206}\text{Pb}$ reservoirs. Utilization of our workflow in the Capricorn Orogen reveals that titanite ages from the same samples as published zircon U–Pb data range from coeval to several hundreds of Myr of age difference between the two minerals. Titanite geochronology and trace element geochemistry indicates ~30 Myr of previously unrecognized prolonged cooling for the Capricorn Orogeny to ca. 1750 Ma. The spatial extent of reworking of the Mutherbukin Tectonic Event is also broadened significantly farther north and south than previously recognized. Incorporating titanite geochronology and trace geochemistry

with more commonly used techniques (e.g., zircon and monazite petrochronology) extends our ability to resolve the complete history of large-scale orogenic terranes.

ACCEPTED MANUSCRIPT

1 INTRODUCTION

Precambrian orogenic belts record complex tectonic and geodynamic histories over large areas. Minerals such as zircon and monazite are often employed as a means of unravelling the evolution of orogenic belts because of their relative ease in obtaining coupled age and geochemical data, their preferential incorporation of U over Pb, and their ability to retain age information due to high-closure temperatures (Hawkesworth and Kemp, 2006; McFarlane and McCulloch, 2007). However, zircon and, to a lesser extent, monazite may not fully capture the geological history of orogenic belts because they do not always participate with metamorphic and hydrothermal fluids (Harley et al., 2007; Rubatto et al., 2001). In order to more fully illuminate the (tectono)thermal history of orogenic belts, it is necessary to investigate other U and Th bearing accessory minerals that more readily participate in metamorphic reactions but still have relatively high closure temperatures.

Titanite (CaTiSiO_5) can host small amounts of uranium in its structure and can therefore be used as a U–Pb geochronometer (Kohn, 2017). Titanite has a relatively high closure temperature for Pb of $\sim 650\text{--}700^\circ\text{C}$, estimated from both empirical (Pidgeon et al., 1996; Scott and St-Onge, 1995; Verts et al., 1996) and experimental observations (Cherniak, 1993). Thus, titanite may record hydrothermal and metamorphic events at temperatures at or just above $\sim 650\text{--}700^\circ\text{C}$ at which other minerals (e.g., zircon and monazite) may still be completely retentive to Pb (Lawley et al., 2014; Rasmussen et al., 2013). However, because recent studies have shown evidence of partial Pb retention for tens of Myr at temperatures of $750\text{--}800^\circ\text{C}$ (Kohn, 2017; Spencer et al., 2013), titanite can sometimes record high-temperature metamorphic events. Titanite is a widespread accessory mineral that can occur in

igneous rocks (calc-alkaline felsic and mafic plutons), metamorphic rocks (calc-silicates, pelites and amphibolites), and may also be present as a detrital component in sedimentary rocks (Frost et al., 2001). Titanite may also incorporate various trace elements which, like zircon and monazite, can be used to reveal the petrogenetic conditions during crystallization (Aleinikoff et al., 2002; Mazdab, 2009).

The main drawback to titanite geochronology is that titanite may incorporate significant concentrations of common-Pb during crystallization due to the similarity of Ca^{2+} and Pb^{2+} ionic radii in the 7-fold coordinated Ca cation site (Kirkland et al., 2017; Kohn, 2017; Shannon, 1976). This means that accurate correction for common-Pb is paramount for obtaining geologically accurate U–Pb ages. Because of this inherent complexity, titanite geochronology has been neglected in favour of zircon and monazite, plus geochronometers with lower closure temperatures such as $^{40}\text{Ar}/^{39}\text{Ar}$ hornblende, mica and feldspar. With the advent of laser ablation inductively coupled mass spectrometry (LA-ICP-MS), it is now possible to cost-effectively collect campaign-style geochronological and geochemical data from across orogen-scale features of the crust (Kylander-Clark et al., 2013; Spencer et al., 2013). This is because the laser ablation method enables rapid, simultaneous acquisition of trace element and isotopic compositions from small volumes.

The incorporation of common-Pb in titanite can also pose a significant problem if a sample records more than one geological event. If a single sample records an igneous crystallization and metamorphic recrystallization event, differentiation between the two is usually possible in a mineral with negligible common-Pb (e.g., zircon) because a discordia line will intercept the U–Pb concordia between the first and second event (e.g., Taylor et al., 2014; Zhang et al.,

2006). However, for a sample with two geological events, any mineral that has significant quantities of common-Pb will yield a triangular envelope that makes it difficult to identify even a single event (Kirkland et al., 2017). Resolving complex titanite age spectra remains a problem that needs to be addressed.

Here, we present results of titanite geochronology and trace element geochemistry of felsic intrusive rocks (meta-granitoids) from the Capricorn Orogen in Western Australia, an orogenic belt that has experienced at least two Paleoproterozoic collisional events and over one billion years of intracontinental reworking (Johnson et al., 2013). Systematic investigation of titanite geochronology and geochemistry data in conjunction with previously obtained geochronological data on other minerals (e.g., zircon) allows us to develop several trace element indices in titanite that may be applied to orogenic terranes that are less well-constrained than the Capricorn Orogen. We also use this new titanite petrochronological data to better understand the tectonic and geodynamic processes that operated during the formation of the Western Australian Craton and its subsequent reworking.

2 GEOLOGICAL BACKGROUND OF THE CAPRICORN OROGEN

The Capricorn Orogen records the protracted tectonothermal geological history of the amalgamation of the West Australian Craton. Composed of Archean–Paleoproterozoic terranes, microcontinents and sedimentary basins, the Capricorn Orogen denotes the suture zones between the Pilbara Craton, Glenburgh Terrane and Yilgarn Craton (Figs. 1 & 2; Cawood and Tyler, 2004; Johnson et al., 2011b; Johnson et al., 2013). With over one billion years of intracontinental reworking and sedimentation spanning most of the Proterozoic, the

complex geological history of the Capricorn Orogen is now subdivided into at least eight distinct tectonothermal events: (i) the 2215–2145 Ma Ophthalmia Orogeny, which sutured the Glenburgh Terrane to the Pilbara Craton (Krapež et al., 2017; Rasmussen et al., 2005), (ii) the 2005–1950 Ma Glenburgh Orogeny, which amalgamated the combined Pilbara Craton–Glenburgh Terrane with the Yilgarn Craton to form the West Australian Craton (Johnson et al., 2010; Johnson et al., 2011b; Occhipinti et al., 2004; Sheppard et al., 2004), (iii) the 1830–1780 Ma Capricorn Orogeny, the first of a series of intracontinental orogenies/tectonic events (Sheppard et al., 2010a), (iv) the 1690–1660 Ma Mangaroon Orogeny (Piechocka et al., 2017; Sheppard et al., 2005), (v) the 1320–1170 Ma Mutherbukin Tectonic Event (Johnson et al., 2011a; Korhonen et al., 2017), (vi) the 1030–990 Ma Edmundian Orogeny (Martin and Thorne, 2004; Piechocka et al., 2017; Sheppard et al., 2007), (vii) the 955–830 Ma Kuparr Tectonic Event (Occhipinti, 2007; Occhipinti and Reddy, 2009; Olierook et al., in review; Piechocka et al., 2017; Piechocka et al., 2018), and (viii) the c. 570 Ma Mulka Tectonic Event (Sheppard et al., 2010b; Wingate and Giddings, 2000).

3 METHODOLOGY

3.1 Sample selection and preparation

Titanite was extracted from 43 meta-granitoid samples from across the Capricorn Orogen; 23 yielded statistically valid ages and five other samples yielded geologically-meaningful estimates. This suite comprised a combination of samples from the archives of the Geological Survey of Western Australia and samples collected during 2014–2016 field campaigns (Figs. 1–2). Four samples were selected from the Sylvania Inlier, an exposed portion of the Pilbara

Craton (Tyler, 1991). Nine samples were analyzed from rocks that have affinity to the Yilgarn Craton including: the Narryer Gneiss Terrane ($n = 1$), the Yarlarweelor Gneiss Complex, a reworked portion of the Narryer Gneiss Terrane ($n = 2$); the Kalgoorlie Terrane ($n = 1$), and; the Marymia Inlier ($n = 2$) and Goodin Inlier ($n = 3$), both probable reworked fragments of the Youanmi Terrane (Mole et al., 2013). Five samples were related to the 2005–1950 Ma Glenburgh Orogeny including the Dalgaringa Supersuite, ($n = 2$), the Nardoo Granite ($n = 1$) and Bertibubba Supersuite, ($n = 2$; Johnson et al., 2011b; Johnson et al., 2013; Occhipinti et al., 2004; Sheppard et al., 2004). Nineteen samples were collected from the Moorarie Supersuite, which comprises predominantly granitic (*sensu lato*) intracontinental plutonism related to the 1830–1780 Ma Capricorn Orogeny (Sheppard et al., 2010a). Six samples were analyzed from the Durlacher Supersuite, a suite of intracontinental granitic plutons emplaced during the 1690–1660 Mangaroon Orogeny (Piechocka et al., 2017; Sheppard et al., 2005). See Table 1 for rock type designation, formation name and precise locations.

Rocks were crushed and their heavy mineral fractions separated using heavy liquids and a Frantz isodynamic magnetic separator. Heavy mineral grains were subsequently hand-picked, mounted in 25 mm epoxy rounds and polished to expose their interiors.

3.2 Titanite imaging

Each mount was imaged using transmitted and reflected light to provide internal grain textural information. Grain mounts were then analyzed using the Tescan Integrated Mineral Analyzer (TIMA), a field emission gun scanning electron microscope (FEG-SEM) housed within at the John de Laeter Centre (JdLC) at Curtin University. Due to its four integrated

energy dispersive X-ray (EDX) detectors, the TIMA enables rapid acquisition of qualitative chemical data, which was used to identify titanite and their inclusion/intergrowth assemblages in heavy mineral populations. Atomic number contrast back scatter electron (BSE) images were then collected using the Tescan Mira3 FEG-SEM from the JdLC using a 12 kV beam current, also at the JdLC. Backscattered electron images were used to document internal zonation patterns (e.g. oscillatory, sector, patchy), identify recrystallization textures and recognize the present of any crystal rims. These identification procedures aid in elucidating whether grains were originally magmatic (igneous), metamorphic or experienced recrystallization.

3.3 In situ U–Th–Pb and trace element analysis

Titanite U–Th–Pb isotopic and trace element measurements were collected using a Resonetics S-155-LR 193 nm excimer laser ablation system coupled to an Agilent 7700x quadrupole mass spectrometer housed within the JdLC at Curtin University. All samples were measured *in situ* from the polished 25 mm epoxy rounds and multiple spots were collected from both grain fragments and individual crystals. A brief overview of operating conditions is given here; for a detailed outline of the LA-ICP-MS instrumentation and techniques, see Kylander-Clark et al. (2013). The laser spot diameter was 33 or 50 μm , the laser fluence was $\sim 1\text{--}4\text{ J cm}^{-2}$, the repetition rate was 3–4 Hz for a 30-second total of 120 shots, which ablates at a rate of 0.05–0.15 μm per pulse. All uncertainties quoted in the text, in tables and in figures are at 2σ .

Analyses of unknowns were bracketed with primary reference materials every ten unknown analyses to monitor and correct for mass fractionation and instrumental drift, including Khan

(522.2 ± 2.2 Ma; Heaman et al., 2002; Kinny et al., 1994) and OLT1 (1014.8 ± 2.0; Kennedy et al., 2010). Secondary standards BLR-1 (1047.1 ± 0.4 Ma; Aleinikoff et al., 2007) and MKED1 (1517.32 ± 0.32 Ma; Spandler et al., 2016) were used to internally monitor data accuracy and precision, and were corrected for mass bias and fractionation based on measured isotopic ratios of the primary reference material using Iolite software (Paton et al., 2011). Precision on individual analyses depend on volume and concentrations of U, Th and Pb, with secondary standards, after normalisation to the primary standard, yielding 1–7% precision on the uncorrected $^{206}\text{Pb}/^{238}\text{U}$ ratios and typically 2–11% precision on the uncorrected $^{207}\text{Pb}/^{206}\text{Pb}$ ratios. The optimum precision for $^{207}\text{Pb}/^{206}\text{Pb}$ vs $^{206}\text{Pb}/^{238}\text{U}$ ratios changes at ca. 2.0 Ga. All titanite weighted mean ages older than 2.0 Ga are presented as $^{207}\text{Pb}/^{206}\text{Pb}$ ages and ages younger than 2.0 Ga are presented as $^{206}\text{Pb}/^{238}\text{U}$ ages. Curtin internal laboratory standard Khan (522.2 ± 2.2 Ma; Heaman, 2009) was used for all titanite trace element concentrations. Khan titanite has been repeatedly characterised by LA-ICPMS (Curtin) and electron probe micro-analysis (Adelaide) for this purpose (see supplemental Table A for element concentrations of Khan titanite). Uncertainties on trace elements in Khan titanite are typically 1.0–1.5% at 2 σ (supplemental Table A). The National Institute of Standards and Technology standard BHVO glass (Kent et al., 2004) was used as a secondary reference material. Trace element data collected on the same titanite grains as U–Pb data, and include Na, Al, V, Cr, Mn, Fe, high field strength elements (HFSE; Y, Zr, Hf, Nb, Ta) and rare earth elements (REE; La–Lu).

All age uncertainties are reported at the 95% confidence interval, assuming a Gaussian distribution of measurement errors. The different distributions of U–Pb dates means that there may be several methods for calculating an age, including a discordia fit through the data, a

concordia age of concordant data only, a weighted mean of uncorrected $^{206}\text{Pb}/^{238}\text{U}$ or $^{207}\text{Pb}/^{206}\text{Pb}$ dates, or a weighted mean of ^{207}Pb -corrected $^{206}\text{Pb}/^{238}\text{U}$ dates. Analyses are considered concordant if they overlap within analytical uncertainty on the $^{207}\text{Pb}/^{206}\text{Pb}$ vs. $^{238}\text{U}/^{206}\text{Pb}$ Tera-Wasserburg concordia curve (Spencer et al., 2016). Because most samples in this study exhibit a broad spread of U/Pb ratios, we use a discordia fit through the uncorrected data, where the y-axis intercept ($^{207}\text{Pb}/^{206}\text{Pb}$) reveals the composition of the common-Pb component and the lower concordia intercept equals the sample age.

There are several instances where a concordia intercept age calculation of all the data (excluding outliers) is not appropriate. First, samples where a statistically-consistent $^{207}\text{Pb}/^{206}\text{Pb}$ intercept was not available ($p < 0.05$) but a linear trend still exists, the regressed intercept is an estimate only. Here, the percentage of common-Pb ($f_{207\%}$) was calculated as an estimate of the amount of non-radiogenic Pb based on the distance from concordance along a projection towards contemporaneous common-Pb. An age estimate is then calculated from uncorrected $^{207}\text{Pb}/^{206}\text{Pb}$ (>2.0 Ga) or $^{206}\text{Pb}/^{238}\text{U}$ (<2.0 Ga) ratios that have $f_{207} < 1\%$ (Kirkland et al., 2018; Kirkland et al., 2017). Secondly, where data do not form a linear trend because all or the majority of data is concordant, a weighted mean of the concordant uncorrected $^{206}\text{Pb}/^{238}\text{U}$ dates or $^{207}\text{Pb}/^{206}\text{Pb}$ dates are calculated; such an approach only applies to one sample (88412) in this study. Lastly, where excess scattering in the U–Pb data occurs that cannot be resolved by titanite textures, no age is calculated.

Zr-in-titanite temperatures were calculated using the method of Hayden et al. (2008).

Although zircon and quartz are commonly observed to coexist with titanite in the analyzed samples, rutile rarely coexists with titanite here. Thus, the activation energy of TiO_2 (a_{TiO_2}) is

lower than 1. Given the plausible limits of $a_{\text{TiO}_2} = 0.5$ in typical crustal rocks (Ferry and Watson, 2007; Hayden and Watson, 2007), the maximum likely overestimation of the crystallization temperature would be ~ 30 °C at temperatures of 500–700 °C and 0.5–1 GPa. Independent geological and P–T–t–x modelling suggests that average pressure estimates are 0.8 GPa for the ca. 2005–1970 Ma Dalgaringa Supersuite (Johnson et al., 2011b), 0.5 GPa for the 1965–1945 Ma Bertibubba Supersuite (Johnson et al., 2011b), 0.4 GPa for the ca. 1830–1780 Ma Capricorn Orogeny (Sheppard et al., 2010a), 0.6 GPa for the ca. 1690–1660 Ma Mangaroon Orogeny (Piechocka et al., 2017; Sheppard et al., 2005) and 0.4 GPa for the ca. 1320–1170 Ma Mutherbukin Tectonic Event (Korhonen et al., 2015; Korhonen et al., 2017). To simplify matters, a constant pressure of 0.5 GPa was used for all data. Temperature estimates may be overestimated by up to 30 °C due to the absence of rutile, and underestimated by up to 30 °C due to higher pressures in the Dalgaringa and Bertibubba Supersuites. To account for this, an uncertainty of ± 30 °C was added to the calculated uncertainty from Zr concentrations and equation uncertainties (Hayden et al., 2008). Full isotopic and trace elemental data set for the samples is given in supplementary Table B.

3.4 Multivariate statistical methods

Principal component analysis (PCA) was undertaken on titanate geochemical data using the statistical analysis software PAST (Hammer et al., 2001). Geochemical data were screened, with spurious spot analyses removed. Data were log-normalised using a centered log-ratio transformation in recognition of the importance of scale invariance with compositional data (Aitchison, 1982) using CoDaPack 2 (Comas Cufí and Thió i Fernández de Henestrosa, 2011) in preparation for multi-dimensional analysis. Using PCA, data dispersion is simplified

to the most significant principal components (PC) with weightings determined for each variable that contributes to the different principle components. The significance of each PC is discussed below with respect to the percent variance of the total dataset that it explains, i.e. the ratio of each PC eigenvalue normalized to the sum of all eigenvalues. The first two PCs account for over 83% of the total data variance (PC1= 69% and PC2= 14%) and are discussed here. Loadings on each element variable and the sample dispersion scores are displayed graphically.

4 RESULTS

Given the quantity of data collected for this study (43 samples), only the salient features are highlighted below. The full results for each of the 43 samples are given in the supplemental material, including BSE images for each titanite type, Tera-Wasserburg and (where applicable) weighted mean plots for the U–Pb data, and brief description of results.

4.1 Titanite grain textures

Backscatter electron analysis of titanite grains within the 43 samples spanning Archean to Neoproterozoic reveal a variety of textures, including sector zoning (Fig. 3a), oscillatory zoning (Fig. 3b), BSE-homogenous grains (Fig. 3c), twinning (supplementary material) and ‘sugary’ alteration (Fig. 3d). The only systematic differences in titanite textures between the different suites in the Capricorn Orogen is that the Archean samples tend to show a greater number of inclusions in titanite grains and more alteration than titanite from Proterozoic samples.

The majority of the textural difference in titanite is related to inclusions/adjoining minerals or whether titanite grains are igneous, recrystallized or metamorphic in origin (confirmed by zircon ages, see section 4.2.1). Igneous grains most commonly show sector zoning (Fig. 3a) or are homogenous in BSE (Fig. 3c) and rarely faint oscillatory zoning (Fig. 3b). Inclusions of zircon are common, particularly from Archean samples. Inclusions or adjacent grains of apatite, feldspar, mica, quartz, amphibole (kaersutite) are also occasionally present in igneous titanite (Fig. 3d–f). Recrystallized titanite grains often show clear cores and rims (Fig. 3g) but are otherwise similar to igneous grains in terms of their internal texture. Metamorphic titanite are predominantly homogenous in BSE and rarely sector-zoned (Fig. 3g–h). Ilmenite inclusions are very common in metamorphic titanite (Fig. 3i).

4.2 Titanite U–Pb geochronology

Of the 43 analyzed samples, 23 yielded statistically-reliable ages (Table 1). The simplest U–Pb spectra display statistically-consistent discordia between a common-Pb upper intercept and a lower intercept with the concordia curve (Fig. 4a, b). The percentage of concordant data in a given sample varies from almost predominantly concordant (~87%) to wholly discordant (Fig. 4a, b). For samples where some scatter exists such that a statistically-consistent discordia line and $^{207}\text{Pb}/^{206}\text{Pb}$ intercept cannot be calculated, it is possible to calculate an age using only points that have negligible common-Pb (i.e., concordant data, Fig. 4c, d). For Proterozoic samples, the discordia line is at high angles to the concordia curve so that this calculation is relatively straightforward (e.g., Fig. 4c). Some Archean titanite U–Pb spectra are significantly more complicated because their linear distribution of U–Pb data between common-Pb and a lower concordia intercept tends to be tangential to the concordia curve

(Fig. 4d). Here, it is best to calculate the percentage of common-Pb and assume negligible common-Pb is defined as $f_{207} < 1\%$ (Fig. 4d).

Still other samples yield widely scattered U–Pb spectra that are not resolvable based on textural criteria alone (Fig. 5). All of the examples shown in Figure 5 may be resolved utilizing trace elemental information, which acts as a powerful discriminant for highlighting different groupings, trends and outliers in U–Pb space (section 4.3). The most appropriate trace element abundances and ratios used to discriminate between titanite dates are REE slope (La/Sm or La/Yb), Th/U, U, Pb and Zr-in-titanite temperatures (Fig. 4, Fig. 5).

The application of trace elements to U–Pb data allow the identification of igneous and subsequent recrystallization events in a single sample (Fig. 5). For example, sample 120644 from the Goodin Inlier yields a main cluster at ca. 2.7–2.6 Ga with high Pb and Zr-in-titanite temperatures trending towards a common-Pb intercept, with a calculated uncorrected $^{207}\text{Pb}/^{206}\text{Pb}$ age of 2644 ± 17 Ma ($f_{207} < 1\%$ only; Fig. 5a). Six additional data with low Zr-in-titanite temperatures and low Pb abundances form a statistically-consistent discordia between the igneous crystallization age and a subsequent recrystallization age of 1850 ± 120 Ma (Fig. 5a). As the upper intercept overlaps with the age for the main cluster and these grains are characterised by decreasing Pb with younger ages, we suggest that these analyses were formed by partial to complete Pb-loss.

It is not always possible to place accurate age constraints on some of these complex U–Pb spectra. For example, titanite U–Pb data in sample 84599 from the Sylvania Inlier reveal a systematic but continuous variation in Th/U ratio with $^{207}\text{Pb}/^{238}\text{U}$ (i.e., the slope of a $^{207}\text{Pb}/^{206}\text{Pb}$ vs. $^{238}\text{U}/^{206}\text{Pb}$ Tera-Wasserburg plot; Fig. 5b). In another example, sample 195826

from the 1690–1660 Ma Durlacher Supersuite is affected by both partial Pb-loss and partial Pb-gain, meaning that it is uncertain if the oldest concordant dates record the igneous crystallization event or are already affected by Pb diffusion (Fig. 5c).

4.2.1 Comparison of titanite U–Pb ages with zircon

All zircon ages for the same samples where titanite was dated have been previously interpreted as recording the igneous crystallization of the rocks (Table 2, Fig. 6). In the majority of cases, calculated titanite ages overlap within 2σ confidence of the published zircon ages (Table 2, Fig. 6a, b). However, several samples from the Paleoproterozoic Moorarie and Durlacher Supersuites revealed ages that were tens of Myr younger than their zircon counterparts (e.g., samples 88412, 88414; Fig. 6b). Still other titanite ages were hundreds of Myr younger than the zircon ages (e.g., samples 190661, 135501; Fig. 6c).

4.3 Titanite trace element geochemistry

The knowledge of titanite textural information (Fig. 3) and differences between U–Pb zircon and U–Pb titanite ages (Fig. 6) provide a robust assignment of whether grains are igneous, recrystallized or metamorphic in most samples. For some analyses, this is not straightforward due to the high U–Pb uncertainties and ambiguous textural information (see supplementary Table B). Here, we interpreted what the most likely origins for these equivocal titanite grains.

4.3.1 Trace element variation with discordance

Uranium and Pb abundances are useful discriminators for assessing whether discordance (i.e., data spread) is a product of common-Pb incorporation or variable common-Pb to radiogenic-Pb ratios. Common-Pb incorporation displays systematic variable Pb and constant U (Fig.

4d), whereas variable common-Pb to radiogenic-Pb is exhibited as constant Pb but systematic variation in U (Fig. 4b). For example, sample 195821 from the Moorarie Supersuite shows higher Pb concentrations closer to the common-Pb intercept, indicative of higher common-Pb away from the lower concordia intercept (Fig. 4d). Conversely, sample 88420 from the Moorarie Supersuite shows increasing U concentrations towards the lower concordia intercept (Fig. 4b). This suggests that the less discordant analyses with more U have higher radiogenic Pb concentrations and more discordant analyses (with less U) have lower radiogenic to common-Pb concentrations.

4.3.2 Trace element variation with igneous, recrystallized and metamorphic grains

The strongest control on titanite trace element geochemistry is whether grains are neocrystallized igneous, recrystallized igneous or neocrystallized metamorphic in origin (Fig. 7). Calculated Zr-in-titanite temperatures, Th/U, Th/Pb, REE slopes, Eu anomalies and Al/(Al+Fe) are all effective criteria for differentiating neocrystallized igneous and metamorphic grains and, to a lesser extent, identifying recrystallized igneous crystals (Fig. 7). Calculated Zr-in-titanite temperatures are most effective at differentiating different titanite grains, yielding average temperatures of 730 °C, 675 °C and 625 °C for igneous, recrystallized and metamorphic titanite, respectively (Fig. 7). In samples where both neocrystallized igneous and recrystallized igneous titanite grains or rims exist, Zr-in-titanite temperatures in the primary domains can be preserved (e.g., sample 195826, Fig. 5c) or lowered due to partial Zr diffusion (e.g., sample 120644, Fig. 5a). However, when all samples are plotted together, there is not always a clear differentiation between neo- and recrystallized

igneous grains (Fig. 7a). Where Zr has diffused out of the crystal lattice, most other trace elements are also reduced in titanite.

Another important chemical index is the proportion of minor elements Al and Fe (Fig. 7b). Although Al varies considerably for neocrystallized igneous, recrystallized igneous or neocrystallized metamorphic titanite, Fe proportions are systematically higher for igneous than for metamorphic titanite (Fig. 7b). As an index, neocrystallized igneous, recrystallized igneous and neocrystallized metamorphic titanite have Al/(Al+Fe) ratios of 0.2–0.6, 0.5–0.8 and 0.9, respectively (Fig. 7c). Thus, Al/(Al+Fe) is particularly effective at differentiating neocrystallized igneous titanite from grains that have experienced interaction with hydrothermal fluids, either through recrystallization or new metamorphic growth.

Th/U and Th/Pb ratios are also useful discriminants of the three titanite types (Fig. 7d,e). Neocrystallized igneous, recrystallized igneous and neocrystallized metamorphic titanite have Th/U ratios of 0.0001–2, 0.05–3, and 0.05–10 (Fig. 7d), and Th/Pb ratios of 0.0001–0.2, 0.05–1 and 0.02–1, respectively (Fig. 7e). Thus, Th/Pb and, to a lesser extent, Th/U is particularly effective at differentiating metamorphic from neo- or recrystallized igneous titanite. When used in conjunction with Zr-in-titanite temperatures or Al/(Al+Fe) indices, the three titanite types are effectively discriminated from each other, although some overlap between neo- and recrystallized igneous titanite still exists (Fig. 7f).

Concentrations and gradients in REE, and Eu anomalies, provide another chemical index to differentiating igneous, recrystallized and metamorphic titanite (Fig. 7g–i). Total abundances of REE (Fig. 7g), the slope of chondrite-normalized (Sun and McDonough, 1989) light to middle rare earth elements (LREE/MREE, [La/Sm]_N, Fig. 7h), light to heavy rare earth

elements (LREE/MREE, $[La/Yb]_n$) and Eu anomaly ($[Eu/Eu^*]_N$, where $Eu^* = \sqrt{[Sm \times Gd]}$; Fig. 7i) vary by several orders of magnitude between samples but rarely vary less than an order of magnitude within an individual sample (see supplemental Table B).

There are exceptions where there may be several orders of magnitude difference in REE concentrations and gradients, particularly where two titanite populations are identified in a single sample (e.g., Fig. 4d). Titanite REE gradients display characteristically negatively sloping for neocrystallized igneous titanite (median $[La/Sm]_N = 25.5$, Fig. 7h, Fig. 8b), whereas recrystallized rims and neocrystallized metamorphic grains have flat to positively sloping REE gradients with median $(La/Sm)_N$ of 1.24 and 0.43, respectively (Fig. 7h, Fig. 8e). Eu anomalies show negative $(Eu/Eu^*)_N$ for both neocrystallized and recrystallized igneous titanite grains (median $[Eu/Eu^*]_N = 0.74$ and 0.63 , respectively, Fig. 8c, f) but positive Eu anomalies for neocrystallized metamorphic grains (median $[Eu/Eu^*]_N = 1.37$, Fig. 8f).

Chemical zonation patterns are also indicative of titanite origin. Magmatic titanite that exhibit oscillatory or sector zoning (Fig. 3) also has corresponding intragrain chemical variations in response to evolving magma compositions. For example, a grain from the 1830–1780 Ma Moorarie Supersuite shows variations in La/Sm and Eu/Eu^* from core to rim (Fig. 9). The variance of REE is only loosely correlated with discordance, implying that Pb is more mobile than REE (Cherniak, 2006). Recrystallized titanite grains show consistently low La/Sm ratios at grain rims but slightly variable Eu/Eu^* that correlates with discordance (Fig. 9).

4.3.3 Spatial and temporal variation in trace elements

There are only subtle differences in titanite trace element abundance and ratios between the five different formations (Fig. 8, Fig. 10b, supplemental Table B). Igneous titanite from the Pilbara Craton, Moorarie Supersuite and Durlacher Supersuite have decreasing concentrations of Th and LREE (supplementary Table B) but these variations may also reflect undersampling of the Pilbara Craton. REE gradients and Eu anomalies are very similar for the Moorarie and Durlacher Supersuites (Fig. 8). Neocrystallized igneous grains have $(\text{La}/\text{Sm})_{\text{N}}$ of 23.6 and 30.9 (Fig. 8b) and $(\text{Eu}/\text{Eu}^*)_{\text{N}}$ of 0.78 and 0.50 for the Moorarie and Durlacher Supersuite, respectively (Fig. 8c). Neocrystallized metamorphic grains have $(\text{La}/\text{Sm})_{\text{N}}$ of 0.72 and 0.85 (Fig. 8e) and $(\text{Eu}/\text{Eu}^*)_{\text{N}}$ of 1.02 and 1.48 for the two supersuites, respectively (Fig. 8f). Thus, the variation in trace elements between geological units is not nearly as evident as the difference between igneous and metamorphic titanite (Fig. 7–9).

4.3.4 Multivariate statistical analysis

A principal component analysis of the titanite trace elements shows that principal components 1 and 2 account for over 83% of the statistical variation (Fig. 10). As a consequence of the high statistical variance captured by just the first two PCs, PC3 and below are not reported. PC1 (69% of the variance) shows that the primary discriminating trace elements are the light to middle REE, Th, Y, Nb, Ta, Al and Mn. PC2 (14% of the variance) is strongly controlled by the middle to heavy REE, Pb, Y, Zr, Fe, V, Mn and Al. Uranium, Eu and Hf have little control on both PC1 and PC2.

PC1 is highly effective at discriminating between igneous and metamorphic titanite, with minimal overlap (Fig. 10a). Igneous titanite consistently have negative PC1 scores and,

conversely, neocrystallized titanite have positive PC2 scores. Recrystallized titanite straddle the middle ground, although with notably low PC2 scores.

The combination of PC1 and PC2 is partly useful at highlighting the Pilbara Craton (low PC1 scores) from the other suites (Fig. 10b). Score differences between the other suites is less clear.

There is no noticeable spatial or geographic control on the PCs for igneous samples from across the Capricorn Orogen. However, we note that most samples were collected from a single tectonic zone (see Fig. 2), so spatial variance may not be fully captured in this study.

5 DISCUSSION

5.1 Interpretation of titanite dates and conversion to geologically-meaningful ages

Titanite dates in a single sample can yield a variety of patterns in U–Pb concordia space, each of which requires a different approach to reveal meaningful geological information (Fig. 11). Here, we discuss the approaches to provide a focussed method to interpreting increasingly complex U–Pb systematics. This approach need not apply only to titanite. Any mineral in an igneous or metamorphic rock that has suitable U–Pb and trace element constituents to allow for petrochronologic analyses can utilize this method.

The majority of samples in this study yield a linear array of U/Pb and Pb/Pb ratios between a $^{207}\text{Pb}/^{206}\text{Pb}$ ordinate intercept and a lower concordia intercept (Fig. 4, ‘igneous titanite’ in Fig. 11). Such trends are relatively simple to interpret as a product of common-Pb incorporation into an otherwise uniform ratio of parent U to daughter radiogenic Pb products (Garber et al.,

2017; Kirkland et al., 2016; Kohn, 2017; Tera and Wasserburg, 1972). It is then straightforward to calculate an age for the sample using the lower concordia intercept (Anand et al., 2014). Where a discordia line cannot be reliably fitted, a weighted mean of uncorrected concordant data can yield an age if all analyses overlap at 2σ uncertainty (e.g., sample 88412, supplementary material; Simonetti et al., 2006; Spencer et al., 2016). Alternatively, if samples still reveal a linear trend towards a $^{207}\text{Pb}/^{206}\text{Pb}$ intercept but are not statistically-valid for a single population, the estimated $^{207}\text{Pb}/^{206}\text{Pb}$ intercept can be used to calculate which concordant analyses have a negligible proportion of common-Pb ($f_{207} < 1\%$, Fig. 4c, d). Given that concordant data are significantly away from the $^{207}\text{Pb}/^{206}\text{Pb}$ intercept (y-axis), an estimate of the $^{207}\text{Pb}/^{206}\text{Pb}$ intercept is sufficient to calculate a reliable age because the choice of common-Pb ratio has negligible impact on data with negligible common-Pb.

It becomes increasingly difficult to determine robust ages when multiple events are recorded in a single sample (Fig. 5). For a sample purported to have two events, U–Pb data will usually define a triangular array (blue region in Fig. 11) where the three endmembers are (i) a $^{207}\text{Pb}/^{206}\text{Pb}$ ordinate common-Pb intercept, (ii) an upper concordia intercept that records the first event (red circle in Fig. 11), and (iii) a lower concordia intercept that records the second event (blue circle in Fig. 11). Establishing the validity of two events requires textural and/or chemical information. For example, sample 84599 shows systematic variation of Th/U with discordia slope ($^{207}\text{Pb}/^{238}\text{U}$; Fig. 5b). The highest Th/U is associated with the igneous event at 2937 ± 67 Ma, whereas the subsequent Mesoproterozoic event has lower Th/U ratios.

Assigning an accurate age to the second event is not possible as the discordia is not well defined. In another example, sample 120644 yields accurate igneous and metamorphic ages that are possible using clear groupings of Pb compositions (Fig. 5a, Fig. 11). Here, igneous

dates are associated with low Pb (< 40 ppm), recrystallized grains have very low Pb (<10 ppm), and grains with significant common-Pb and older apparent dates have high Pb (>60 ppm). In a final example, sample 195826 partially mimics sample 120644 in that it has clear upper and lower discordia intercepts (Fig. 5c, Fig. 11). However, sample 195826 also yielded a significant number of discordant U–Pb data that have lost Zr and Pb with respect to their concordant equivalents. Because of the lack of distinct clustering at both upper and lower intercepts, the oldest (~1.6 Ga) and youngest (~1.2 Ga) concordant spots are minimum and maximum ages for the first and second event, respectively. Nevertheless, these three examples show that it is possible to extract valuable geological information from titanite grains despite the issues of Pb mobility and incorporation of common Pb.

It should be noted that three or more events are very unlikely to be readily decipherable in any titanite samples unless they can be clearly linked to textural information (e.g., grain core with multiple rims).

5.2 Application of chemical indices to differentiation of igneous, recrystallized and neocrystallized metamorphic phases

Regional geochronological data from the Capricorn Orogen allow titanite dates to be tied to well-constrained tectonothermal events (Fig. 6). Distinction of igneous vs. metamorphic origin for titanite have also been made in other regions that have experienced multiple tectonothermal events, such as the Western Gneiss Region in Norway (Garber et al., 2017), East Greenland (Kirkland et al., 2017) and the Glastonbury Complex, USA (Aleinikoff et al., 2002). Our results demonstrate that Zr-in-titanite thermometry, REE slope and Eu anomalies, Al/(Al+Fe), Th/U and Th/Pb are the primary chemical indices to effectively discriminate

between neocrystallized igneous, recrystallized igneous, and neocrystallized metamorphic titanite grains from the Capricorn Orogen (Fig. 7, Fig. 10). Each of these indices are discussed in turn.

Zirconium and Ti are important elements that can substitute for each other to a limited extent in titanite, rutile and zircon (Ferry and Watson, 2007; Hayden et al., 2008; Tomkins et al., 2007; Zack et al., 2004). The amount of substitution is primarily controlled by temperature and pressure but is also sensitive to co-crystallization of other Si-, Ti- and Zr-bearing phases, and deformation (Hayden et al., 2008; Timms et al., 2011; Watson et al., 2006). Igneous grains are consistently between 680–820 °C, compatible with the titanite Pb closure temperature of 750–800 °C (Kohn, 2017; Spencer et al., 2013). Lower values of Zr-in-titanite temperatures from ~580 to 740 °C for igneous grains are associated predominantly with grains from the Yilgarn Craton and Moorarie Supersuite (Fig. 7a). This may be a result of (a) misidentification of igneous titanite, (b) incorrect calculation of temperature, particularly if there is no rutile buffer in the sample or the used pressure of 0.5 GPa is too low for Yilgarn Craton and Moorarie Supersuite (Hayden et al., 2008), (c) closure temperature has been affected, or (d) recrystallization of titanite and redistribution of trace elements due to subsequent events. Recrystallized igneous titanite grains consistently record lower crystallization temperatures than igneous grains, but not as low as neocrystallized metamorphic grains, implying partial mobility of Zr during the same event(s) that resulted in near to complete Pb-loss (Cherniak, 1993, 2006). Zr-in-titanite temperatures of 560–640 °C in neocrystallized metamorphic grains are compatible with lower to upper amphibolite facies, which are compatible with temperatures that have been independently constrained for the 1690–1660 Ma Mangaroon Orogeny, 1320–1170 Ma Mutherbukin Tectonic Event and 1030–

990 Ma Edmondian Orogeny (Korhonen et al., 2015; Korhonen et al., 2017; Piechocka et al., 2017; Sheppard et al., 2005; Sheppard et al., 2007).

Both Al^{3+} and Fe^{3+} can substitute for Ti^{4+} in the octahedral (Ti) site, together with a replacement of O^{2-} with F^- or OH^- to accommodate the charge balance (Franz and Spear, 1985; Higgins and Ribbe, 1976; Oberti et al., 1991). Although Al varies considerably regardless of the type of titanite, the amount of Fe is significantly lower for neocrystallized metamorphic titanite (Fe = 2000–7200 ppm) than neocrystallized and recrystallized igneous titanite (Fe = 7000–18000 ppm; Fig. b, c). The incorporation of Al and Fe is facilitated by the similar ionic radii of Ti^{4+} (0.605 Å), Al^{3+} (0.535 Å) and Fe^{3+} (0.645 Å) at the octahedral site (Shannon, 1976). The larger ionic radius of Fe^{3+} means that it is able to readily substitute for Ti^{4+} at higher temperatures (i.e., igneous) but struggles to do so at lower temperatures (i.e., metamorphic conditions). During neocrystallization of metamorphic titanite, the smaller radius of Al^{3+} is preferentially favoured over Fe^{3+} in the octahedral site, which explains the higher Al/(Al+Fe) index for metamorphic titanite (Fig. 7). Recrystallized igneous grains express intermediate Al/(Al+Fe) index values between igneous and neocrystallized metamorphic grains, which probably reflects some added incorporation of Al during recrystallization.

The ratios of Th/U and Th/Pb are primarily controlled by the partition coefficients of Th and U in different co-crystallizing minerals in magmatic and metamorphic systems and, to a lesser extent, temperature (Fig. 7d, e; Prowatke and Klemme, 2005; Tiepolo et al., 2002). The co-crystallization of monazite in particular can act as a Th (and REE) sink, causing lower Th/U and Th/Pb ratios. From nearby samples within the same units, monazite is commonly

observed and dated coeval with titanite in the 1320–1170 Ma Mutherbukin Tectonic Event where most metamorphic titanite ages from this study are recorded (Korhonen et al., 2015; Korhonen et al., 2017). Another important control on the Th/Pb ratio is the higher diffusivity of Pb relative to Th (Cherniak, 1993, 2010). Neocrystallized and recrystallized igneous titanite has comparable Th compositions as a function of melt chemistry but Pb concentrations are significantly lower for recrystallization titanite. Radiation damage from the decay of Th or U to Pb is annealed readily at high temperatures but damage is less rapidly repaired at lower temperatures associated with greenschist and amphibolite facies metamorphism such as is observed in the Capricorn Orogen (Cherniak, 1993). Thus, recrystallization is able to diffuse out Pb more effectively than Th, yielding high Th/Pb ratios for recrystallized titanite and progressively lower Th/Pb ratios for higher-temperature igneous titanite (Fig. 7e). A final complication in the interpretation of Th/U and Th/Pb ratios is the incorporation of common-Pb during crystallization. As a function of ionic radius, Pb is more readily incorporated during higher temperature than lower temperature crystallization (Tiepolo et al., 2002), which explains the anomalously high Pb concentrations in some igneous grains (up to 30000 ppm) and low to negligible Pb concentrations from metamorphic titanite in this study and others (e.g., Garber et al., 2017). This is another mechanism to explain the low Th/Pb ratios of some high-temperature igneous grains that have not experienced recrystallization. The relative incorporation of Th and U, higher diffusivity of Pb than Th and higher incorporation of Pb in higher temperatures together explain the observed convex-upwards relationship between Th/Pb and Zr-in-titanite temperatures in the Capricorn Orogen (Fig. 7d, e). However, we stress that the mechanisms governing the Th/U and Th/Pb ratios are relatively complex. Because of this complexity, it may be that the use of Th/U and

Th/Pb indices for differentiating igneous, recrystallized and metamorphic titanite may not be as effective in other terranes as it is in the Capricorn Orogen.

The incorporation of REE in the 7-fold coordinate Ca site is a product of similar ionic radii of REE³⁺ (La³⁺ = 1.10 Å to Lu³⁺ = 0.93 Å) and Ca²⁺ (1.06 Å; Shannon, 1976). The incorporation of total REE contents is primarily controlled by the fluid or melt composition during crystallization and the ability for trace elements to substitute for mineral-forming elements at different temperatures and pressures (Fig. 7g; Tiepolo et al., 2002). Igneous titanite can show concentric zoning in trace elements – particularly REE – resulting in up to an order of magnitude intragrain variability that increases or decreases relatively linearly from core to rim (Fig. 9a). However, neocrystallised metamorphic titanite appears relatively homogenous presumably (Fig. 9b). The reason for REE homogeneity is that the fluid chemistry during subsequent metamorphic reactions is more homogenous than magma, which experiences fractional crystallization and mixing from replenishing magma or wall rock assimilation. The ratio of trivalent lighter to heavier REE is controlled by temperature, specifically by the preferential uptake of REE with ionic radii that are at or smaller than Ca²⁺ (Garber et al., 2017; Tiepolo et al., 2002). At higher temperatures, LREE to MREE are preferentially incorporated over HREE, whereas at lower temperatures MREE to HREE are more dominant, an interpretation that is corroborated by positive correlation between Zr-in-titanite temperature and (La/Sm)_N (Fig. 7h). Another important observation is the significant difference of (La/Sm)_N ratios between neocrystallized igneous grains and recrystallized igneous grains (Fig. 8b,e), implying that LREE are more readily transferred to the formation fluids during metamorphism, whereas MREE and HREE are relatively immobile.

The use of Eu anomalies also deserve mention, as Eu/Eu^* is systematically positive at lower temperatures and negative at higher temperatures (Fig. 7i, Fig. 8c,f). Chondrite-normalized Ce anomalies are negligible regardless of crystallization temperature (see supplementary Table B), implying that changes in redox conditions cannot explain the Eu anomaly phenomenon. Rather, igneous titanite has negative Eu/Eu^* because of plagioclase fractionation incorporating Eu^{2+} from the melt. The generation of metamorphic titanite is probably accommodated by the breakdown of this Eu^{2+} -bearing plagioclase (Fig. 3f) that then generates positive Eu anomalies. There is no noticeable difference in negative Eu anomalies between neocrystallized and recrystallized igneous grains, implying that Eu is relatively immobile during partial Pb loss.

The use of chemical indices as discussed above in differentiating neocrystallized igneous, recrystallized igneous and neocrystallized metamorphic titanite is exemplified in sample 81867. The zircon age for this sample (3187 ± 50 Ma) overlaps within uncertainty of the titanite age (3202 ± 58 Ma; Table 2). Although both these estimates are imprecise, the simplest interpretation is that the titanite is magmatic. However, titanite from this sample has average Zr-in-titanite temperatures of 662 ± 13 °C, $\text{Al}/(\text{Al}+\text{Fe})$ ratios of 0.7, $(\text{La}/\text{Yb})_{\text{N}}$ ratios of 1 and Th/Pb ratios of 0.13; all of these characteristics are more compatible with a recrystallized igneous origin. While the geochronological information suggests that the titanite and zircon ages are likely coeval, the trace elements indicates that the titanite grains have been recrystallized shortly after the crystallization of the protolith, which would be unresolvable with traditional geochronology.

5.3 Common-Pb reservoir in the Capricorn Orogen

Titanite is particularly susceptible to the incorporation of common-Pb during crystallization. In particular, Pb will exchange with the 7-fold coordinated Ca cations during titanite crystallization (Kirkland et al., 2016). The ordinate intercept of the U–Pb data on a Tera–Wasserburg concordia plot allows the determination of the initial $^{207}\text{Pb}/^{206}\text{Pb}$ ratio of the common-Pb component (Kirkland et al., 2018; Kirkland et al., 2017; Tera and Wasserburg, 1972).

The $^{207}\text{Pb}/^{206}\text{Pb}$ ratio of common-Pb in titanite grains from the Capricorn Orogen is, at times, significantly more radiogenic than expected from a terrestrial common-Pb model (Kirkland et al., 2017; Stacey and Kramers, 1975). Precise $^{207}\text{Pb}/^{206}\text{Pb}$ intercepts from the ca. 1830–1780 Ma Moorarie Supersuite consistently exhibit ratios of ~ 0.8 that are more radiogenic than would be predicted in Stacey and Kramers (1975) model of ~ 0.98 (Table 1). The implication is that a uniform radiogenic reservoir, or homogeneously mixed radiogenic–terrestrial reservoir, was tapped to form titanite in the Moorarie Supersuite. Similarly, the ca. 1690–1660 Ma Durlacher Supersuite reveals $^{207}\text{Pb}/^{206}\text{Pb}$ intercepts of 0.57–0.69, far more radiogenic than predicted terrestrial common-Pb values of 0.96–0.97 (Stacey and Kramers, 1975). In fact, only in a handful of samples are the $^{207}\text{Pb}/^{206}\text{Pb}$ intercepts similar to the terrestrial common-Pb reservoir, indicative of an orogen-scale process that has introduced radiogenic inherited common-Pb into neo- or recrystallized titanite grains.

Another notable observation is the incorporation of at least two common-Pb reservoirs into a single sample. Sample 84577 highlights this well, showing with $^{207}\text{Pb}/^{206}\text{Pb}$ intercepts of <0.4 and >0.7 (Fig. 4d). Note that these $^{207}\text{Pb}/^{206}\text{Pb}$ intercepts are maximum and minimum

estimates only; the true common-Pb reservoirs may have $^{207}\text{Pb}/^{206}\text{Pb}$ ratios below 0.4 and above 0.7.

5.4 Implications for the geological history the Capricorn Orogen

New, statistically-reliable data for titanite and published geochronological data for zircon from the same samples in the Sylvania Inlier, Moorarie Supersuite and Durlacher Supersuite predominantly overlap in age within 2σ uncertainty (Fig. 6, Table 2). However, several titanite ages from samples related to the 1830–1780 Ma Capricorn Orogeny are several tens of Myr younger than their zircon counterparts, with no apparent spatial control on age distribution (Fig. 6, Fig. 12). Moreover, these ages are also younger (ca. 1750 Ma) than the previously published temporal range of the Capricorn Orogeny (Sheppard et al., 2010a). The variation of Eu/Eu^* and LREE/HREE from the centre to outside of titanite grains (e.g., Fig. 9a) indicates that these grains are igneous, with the variation attributed to changing magma chemistry during crystallization (Piccoli et al., 2000). The trace element chemical indices also strongly indicate a neocrystallized igneous origin. Moreover, the titanite growth temperature of titanite ($\sim 750\text{--}800\text{ }^\circ\text{C}$) is consistently higher than the amphibolite facies conditions that occurred during the Capricorn Orogeny, precluding a metamorphic origin for the zircon–titanite age divergence (Sheppard et al., 2010a). The most plausible explanation is that the Moorarie Supersuite experienced a prolonged (i.e., slow) cooling history from the crystallization of the granitoids as indicated by the closure temperature of zircon ($>1000\text{ }^\circ\text{C}$) and the closure of titanite ($\sim 750\text{ }^\circ\text{C}$). At least some regions in the Capricorn Orogen experienced a prolonged cooling history elevated until ca. 1750 Ma, which is ~ 30 Myr longer

than previously recognised for the 1830–1780 Ma Capricorn Orogeny (Sheppard et al., 2010a).

Nine samples yielded titanite ages that are several hundred of Myr younger than their zircon counterparts, probably reflecting that zircon records the igneous crystallization and titanite subsequent metamorphic reworking (Fig. 6, Table 2). One additional sample from the Goodin Inlier (120644) also yielded metamorphic ages of 1850 ± 120 Ma in addition to 2644 ± 17 Ma, the latter of which is expected for the igneous crystallization of this part of the Yilgarn Craton (Mole et al., 2013). The ten samples that record younger titanite ages than zircon ages are found in all rock suites across the Capricorn Orogen, illustrating the ubiquity of post-crystallization metamorphism (Fig. 12).

The majority of titanite ages that are hundreds of Myr younger than zircon ages broadly fall into three groups, each of which is associated with a previously recognized tectonothermal event in the Capricorn Orogen. One sample from the Goodin Inlier (120644) records an age of 1850 ± 120 Ma, which is most likely associated with the 1830–1780 Ma Capricorn Orogeny (Sheppard et al., 2010a). One sample from the Moorarie Supersuite (135433) probably records a latest Paleoproterozoic age (supplemental data) that is most likely associated with the 1690–1660 Ma Mangaroon Orogeny (Piechocka et al., 2017; Sheppard et al., 2005).

Most other samples record ages spanning between ca. 1250 and 1110 Ma (Fig. 6, Table 2), overlapping within 2σ of zircon, monazite and xenotime ages that record the final stages of the 1320–1170 Ma Mutherbukin Tectonic Event (Johnson et al., 2011a; Korhonen et al., 2015; Korhonen et al., 2017). The second stage of the Mutherbukin Tectonic Event, dated

using zircon at ca. 1210–1170 Ma, is interpreted as reaching peak temperature conditions of >650 °C in the south and <550 °C in the northern part of the Mutherbukin Zone (see Fig. 2 for location; Korhonen et al., 2015; Korhonen et al., 2017). Given that most of these samples that record a metamorphic age were from the Limejuice Zone (north of the Mutherbukin Zone; Fig. 12), the calculated Zr-in-titanite temperatures of 560–640 °C in neocrystallized grains are compatible with amphibolite facies metamorphism during the Mutherbukin Tectonic Event. Thus, titanite, together with some monazite and xenotime, probably grew during retrogressive metamorphic stages at ca. 1170 Ma (Korhonen et al., 2017).

Interestingly, several of the samples that record a Mutherbukin-aged event are situated in the Limejuice Zone and along the southern margin of the Capricorn Orogen (Fig. 2). The Mutherbukin Tectonic Event was so named because it was thought to be restricted to the Mutherbukin Zone (Johnson et al., 2011a). Our dates further north and south suggest that the Mutherbukin Tectonic Event was not as restricted as previously thought (Korhonen et al., 2015; Korhonen et al., 2017).

Two other samples yielded ages of 959 ± 88 and 863 ± 65 Ma from the Durlacher and Moorarie Supersuites, respectively. Both events may be associated with the ca. 955–830 Ma Kuparr Tectonic Event (Olierook et al., in review). Given their relatively imprecise errors, the former age may instead record the ca. 1030–990 Ma Edmundian Orogeny (Sheppard et al., 2007).

6 CONCLUSIONS

Geochronology and trace element geochemistry of 43 titanite samples across the western Capricorn Orogen have revealed complex U–Pb arrays that can be interpreted by discerning proportions of common-Pb and Pb-loss (Fig. 11). Of these 43 samples, 23 samples yielded data that could be used to calculate statistically-valid ages. In interpreting titanite, it is important to recognize components of common-Pb and multiple (re)crystallization events to effectively convert U–Pb dates to geologically meaningful ages:

- (1) Samples that have experienced single igneous or metamorphic events are characterized by concordant dates and a linear trend of discordant data with variable incorporation of common-Pb of a single composition.
- (2) Samples with two events show a more complex U–Pb triangular envelope that can be differentiated into two distinct events on the basis of titanite textures, U–Pb spectra and chemical compositions. The recognition of incorporated radiogenic common-Pb is important, particularly in geochronological applications to accurately account and correct for minerals that tend to incorporate significant amounts of common-Pb.

Trace element chemistry in titanite is effective at differentiating between neocrystallized igneous, recrystallized igneous and neocrystallized metamorphic titanite. The most effective indices are Zr-in-titanite temperature, $Al/(Al+Fe)$, Th/U and Th/Pb ratios, REE gradients and Eu anomalies. Given the complex conditions that govern Th/U and Th/Pb ratios, these two indices may not be effective chemical indices for other terranes.

For the Capricorn Orogen, the comparison of titanite ages with published zircon ages reveal coeval to several hundreds of Myr of age difference between the two minerals. Titanite

geochronology and trace element geochemistry reveals previously unrecognized prolonged cooling to ca. 1750 Ma of the 1830–1780 Capricorn Orogeny. The 1320–1170 Ma Mutherbukin Tectonic Event is also shown to occur into the Limejuice Zone to the north of the Mutherbukin Zone and along the southern margin of the Capricorn Orogen, expanding the previously known spatial extent of this Mesoproterozoic tectonothermal event.

Ultimately, titanite geochronology and geochemistry can be valuable tools for understanding the full geologic history of complex orogenic belts.

Acknowledgements

This research was funded by the Science and Industry Endowment Fund as part of The Distal Footprints of Giant Ore Systems: UNCOVER Australia Project (RP04-063) — Capricorn Distal Footprints. Benjamin P. Wade is thanked for assistance and discussions regarding the acquisition and interpretation of trace element data. We thank reviewers D. Chew and J. N. Aleinikoff, and editor B. S. Kamber for the detailed and constructive comments that improved the manuscript.

References

- Aitchison, J., 1982. The statistical analysis of compositional data. *Journal of the Royal Statistical Society. Series B (Methodological)*, 139-177.
- Aleinikoff, J.N., Wintsch, R.P., Fanning, C.M., Dorais, M.J., 2002. U–Pb geochronology of zircon and polygenetic titanite from the Glastonbury Complex, Connecticut, USA: an integrated SEM, EMPA, TIMS, and SHRIMP study. *Chemical Geology* 188, 125-147.
- Aleinikoff, J.N., Wintsch, R.P., Tollo, R.P., Unruh, D.M., Fanning, C.M., Schmitz, M.D., 2007. Ages and origins of rocks of the Killingworth dome, south-central Connecticut: Implications for the tectonic evolution of southern New England. *American Journal of Science* 307, 63-118.
- Anand, R., Balakrishnan, S., Kooijman, E., Mezger, K., 2014. Neoproterozoic crustal growth by accretionary processes: Evidence from combined zircon–titanite U–Pb isotope studies on granitoid rocks around the Hutti greenstone belt, eastern Dharwar Craton, India. *Journal of Asian Earth Sciences* 79, 72-85.
- Bodorkos, S., Love, G.J., Nelson, D.R., Wingate, M.T.D., 2006a. 88411: biotite granodiorite, Bentley Well; Geochronology dataset 610, Compilation of geochronology data, June 2006 update. Western Australia Geological Survey, pp. 1-4.
- Bodorkos, S., Love, G.J., Nelson, D.R., Wingate, M.T.D., 2006b. 88414: porphyritic monzogranite, Nurunah Hill; Geochronology dataset 612, Compilation of geochronology data, June 2006 update. Western Australia Geological Survey, pp. 1-4.

- Bodorkos, S., Love, G.J., Nelson, D.R., Wingate, M.T.D., 2006c. 88415: porphyritic granodiorite dyke, Nurunah Hill; Geochronology dataset 613, Compilation of geochronology data, June 2006 update. Western Australia Geological Survey, pp. 1-4.
- Bodorkos, S., Love, G.J., Wingate, M.T.D., 2006d. 88405: biotite granodiorite, Harvey Well; Geochronology dataset 606, Compilation of geochronology data, June 2006 update. Western Australia Geological Survey, pp. 1-4.
- Bodorkos, S., Love, G.J., Wingate, M.T.D., 2006e. 88407: porphyritic monzogranite, Dunnise Well; Geochronology dataset 607, Compilation of geochronology data, June 2006 update. Western Australia Geological Survey, pp. 1-4.
- Bodorkos, S., Love, G.J., Wingate, M.T.D., 2006f. 88412: foliated porphyritic monzogranite, Bentley Well; Geochronology dataset 611, Compilation of geochronology data, June 2006 update. Western Australia Geological Survey, pp. 1-4.
- Bodorkos, S., Love, G.J., Wingate, M.T.D., 2006g. 88420: biotite granodiorite, Hatches Soak; Geochronology dataset 615, Compilation of geochronology data, June 2006 update. Western Australia Geological Survey, pp. 1-4.
- Cawood, P.A., Tyler, I.M., 2004. Assembling and reactivating the Proterozoic Capricorn Orogen: lithotectonic elements, orogenies, and significance. *Precambrian Research* 128, 201-218.
- Cherniak, D.J., 1993. Lead diffusion in titanite and preliminary results on the effects of radiation damage on Pb transport. *Chemical Geology* 110, 177-194.

- Cherniak, D.J., 2006. Zr diffusion in titanite. *Contributions to Mineralogy and Petrology* 152, 639-647.
- Cherniak, D.J., 2010. Diffusion in Accessory Minerals: Zircon, Titanite, Apatite, Monazite and Xenotime. *Reviews in Mineralogy and Geochemistry* 72, 827-869.
- Comas Cufí, M., Thió i Fernández de Henestrosa, S., 2011. CoDaPack 2.0: a stand-alone, multi-platform compositional software, in: Egozcue, J.J., Tolosana-Delgado, R., Ortego, M.I. (Eds.), *CoDaWork'11: 4th International Workshop on Compositional Data Analysis*, Sant Feliu de Guíxols, Spain.
- Ferry, J.M., Watson, E.B., 2007. New thermodynamic models and revised calibrations for the Ti-in-zircon and Zr-in-rutile thermometers. *Contributions to Mineralogy and Petrology* 154, 429-437.
- Franz, G., Spear, F.S., 1985. Aluminous titanite (sphene) from the Eclogite Zone, south-central Tauern Window, Austria. *Chemical Geology* 50, 33-46.
- Frost, B.R., Chamberlain, K.R., Schumacher, J.C., 2001. Sphene (titanite): phase relations and role as a geochronometer. *Chemical Geology* 172, 131-148.
- Garber, J.M., Hacker, B.R., Kylander-Clark, A.R.C., Stearns, M., Seward, G., 2017. Controls on Trace Element Uptake in Metamorphic Titanite: Implications for Petrochronology. *Journal of Petrology* 58, 1031-1057.
- Hammer, Ø., Harper, D., Ryan, P., 2001. PAST: Paleontological Statistics Software Package for Education and Data Analysis Palaeontol. *Electronica* 4: 1-9.

- Farver, J.R., Kelley, S.P., Miller, A., 2007. Zircon Behaviour and the Thermal Histories of Mountain Chains. *Elements* 3, 25-30.
- Hawkesworth, C.J., Kemp, A.I.S., 2006. Using hafnium and oxygen isotopes in zircons to unravel the record of crustal evolution. *Chemical Geology* 226, 144-162.
- Hayden, L.A., Watson, E.B., 2007. Rutile saturation in hydrous siliceous melts and its bearing on Ti-thermometry of quartz and zircon. *Earth and Planetary Science Letters* 258, 561-568.
- Hayden, L.A., Watson, E.B., Wark, D.A., 2008. A thermobarometer for sphene (titanite). *Contributions to Mineralogy and Petrology* 155, 529-540.
- Heaman, L.M., 2009. The application of U–Pb geochronology to mafic, ultramafic and alkaline rocks: An evaluation of three mineral standards. *Chemical Geology* 261, 43-52.
- Heaman, L.M., Srivastava, R.K., Sinha, A.K., 2002. A precise U-Pb zircon/baddeleyite age for the Jasra igneous complex, Karbi-Analong District, Assam, NE India. *Current Science* 82, 744-748.
- Higgins, J.B., Ribbe, P.H., 1976. The crystal chemistry and space groups of natural and synthetic titanites. *American Mineralogist* 61, 878-888.
- Jahn, I., in review. Crustal evolution of the Capricorn Orogen, Western Australia, Department of Applied Geology. Curtin University, Perth.

- Johnson, S., Sheppard, S., Thorne, A., Rasmussen, B., Fletcher, I., Wingate, M., Cutten, H., 2011a. The role of the 1280–1250 Ma Mutherbukin Tectonic Event in shaping the crustal architecture and mineralization history of the Capricorn Orogen. GSWA 2011 extended abstracts: promoting the prospectivity of Western Australia, 1-3.
- Johnson, S.P., Sheppard, S., Rasmussen, B., Wingate, M.T.D., Kirkland, C.L., Muhling, J.R., Fletcher, I.R., Belousova, E., 2010. The Glenburgh Orogeny as a record of Paleoproterozoic continent–continent collision. Geological Survey of Western Australia, Report 2010/5, 54p.
- Johnson, S.P., Sheppard, S., Rasmussen, B., Wingate, M.T.D., Kirkland, C.L., Muhling, J.R., Fletcher, I.R., Belousova, E.A., 2011b. Two collisions, two sutures: Punctuated pre-1950 Ma assembly of the West Australian Craton during the Ophthalmian and Glenburgh Orogenies. *Precambrian Research* 189, 239-262.
- Johnson, S.P., Thorne, A.M., Tyler, I.M., Korsch, R.J., Kennett, B.L.N., Cutten, H.N., Goodwin, J., Blay, O., Blewett, R.S., Joly, A., Dentith, M.C., Aitken, A.R.A., Holzschuh, J., Salmon, M., Reading, A., Heinson, G., Boren, G., Ross, J., Costelloe, R.D., Fomin, T., 2013. Crustal architecture of the Capricorn Orogen, Western Australia and associated metallogeny. *Australian Journal of Earth Sciences* 60, 681-705.
- Kennedy, A.K., Kamo, S.L., Nasdala, L., Timms, N.E., 2010. Grenville skarn titanite: potential reference material for SIMS U–Th–Pb analysis. *The Canadian Mineralogist* 48, 1423-1443.

- Kent, A.J.R., Jacobsen, B., Peate, D.W., Waight, T.E., Baker, J.A., 2004. Isotope Dilution MC-ICP-MS Rare Earth Element Analysis of Geochemical Reference Materials NIST SRM 610, NIST SRM 612, NIST SRM 614, BHVO-2G, BHVO-2, BCR-2G, JB-2, WS-E, W-2, AGV-1 and AGV-2. *Geostandards and Geoanalytical Research* 28, 417-429.
- Kinny, P., McNaughton, N., Fanning, C., Maas, R., 1994. 518 Ma sphene (titanite) from the Khan pegmatite, Namibia, southwest Africa: a potential ion-microprobe standard, Eighth International Conference on Geochronology, Cosmochronology and Isotope Geology Abstracts: Berkeley, US Geological Survey Circular, p. 171.
- Kirkland, C.L., Fougereuse, D., Reddy, S.M., Hollis, J., Saxey, D.W., 2018. Assessing the mechanisms of common Pb incorporation into titanite. *Chemical Geology* 483, 558-566.
- Kirkland, C. ., olli s, J., Danišik, ., P etersen, J., Evans, N.J., McDonald, B.J., 2017. Apatite and titanite from the Karrat Group, Greenland; implications for charting the thermal evolution of crust from the U-Pb geochronology of common Pb bearing phases. *Precambrian Research* 300, 107-120.
- Kirkland, C.L., Spaggiari, C.V., Johnson, T.E., Smithies, R. ., Da nišik, ., Eva ns, ., Wingate, M.T.D., Clark, C., Spencer, C., Mikucki, E., McDonald, B.J., 2016. Grain size matters: Implications for element and isotopic mobility in titanite. *Precambrian Research* 278, 283-302.

- Kohn, M.J., 2017. Titanite Petrochronology. *Reviews in Mineralogy and Geochemistry* 83, 419-441.
- Korhonen, F.J., Johnson, S.P., Fletcher, I.R., Rasmussen, B., Sheppard, S., Muhling, J.R., Dunkley, D.J., Wingate, M.T.D., Roberts, M.P., Kirkland, C.L., 2015. Pressure-temperature-time evolution of the Mutherbukin Tectonic Event, Capricorn Orogen. Geological Survey of Western Australia, Report 146, p. 70 p.
- Korhonen, F.J., Johnson, S.P., Wingate, M.T.D., Kirkland, C.L., Fletcher, I.R., Dunkley, D.J., Roberts, M.P., Sheppard, S., Muhling, J.R., Rasmussen, B., 2017. Radiogenic heating and craton-margin plate stresses as drivers for intraplate orogeny. *Journal of Metamorphic Geology* 35, 631-661.
- Krapež, B., Ülker, S.G., Fletcher, I.R., Rasmussen, B., 2017. A tale of two basins? Stratigraphy and detrital zircon provenance of the Palaeoproterozoic Turee Creek and Horseshoe basins of Western Australia. *Precambrian Research* 294, 67-90.
- Kylander-Clark, A.R.C., Hacker, B.R., Cottle, J.M., 2013. Laser-ablation split-stream ICP petrochronology. *Chemical Geology* 345, 99-112.
- Lawley, C.J.M., Selby, D., Condon, D., Imber, J., 2014. Palaeoproterozoic orogenic gold style mineralization at the Southwestern Archaean Tanzanian cratonic margin, Lupa Goldfield, SW Tanzania: Implications from U–Pb titanite geochronology. *Gondwana Research* 26, 1141-1158.

- Martin, D.M., Thorne, A.M., 2004. Tectonic setting and basin evolution of the Bangemall Supergroup in the northwestern Capricorn Orogen. *Precambrian Research* 128, 385-409.
- Mazdab, F.K., 2009. Characterization of flux-grown trace-element-doped titanite using the high-mass-resolution ion microprobe (SHRIMP-RG). *The Canadian Mineralogist* 47, 813-831.
- McFarlane, C.R.M., McCulloch, M.T., 2007. Coupling of in-situ Sm–Nd systematics and U–Pb dating of monazite and allanite with applications to crustal evolution studies. *Chemical Geology* 245, 45-60.
- Mole, D.R., Fiorentini, M.L., Cassidy, K.F., Kirkland, C.L., Thebaud, N., McCuaig, T.C., Doublier, M.P., Duuring, P., Romano, S.S., Maas, R., Belousova, E.A., Barnes, S.J., Miller, J., 2013. Crustal evolution, intra-cratonic architecture and the metallogeny of an Archaean craton. Geological Society, London, Special Publications 393.
- Nelson, D.R., 2004. 169090: porphyritic biotite monzogranite, Hogan Well; Geochronology dataset 46, Compilation of geochronology data, June 2006 update. Western Australia Geological Survey, pp. 1-6.
- Nelson, D.R., 2005. 178024: biotite granodiorite, Minga Well; Geochronology dataset 533, Compilation of geochronology data, June 2006 update. Western Australia Geological Survey, pp. 1-4.
- Oberti, R., Smith, D.C., Rossi, G., Caucia, F., 1991. The crystal-chemistry of high-aluminium titanites. *European Journal of Mineralogy*, 777-792.

- Occhipinti, S.A., 2007. Neoproterozoic reworking in the Paleoproterozoic Capricorn Orogen: evidence from $40\text{Ar}/39\text{Ar}$ ages. *Geological Survey of Western Australia Record* 2007/10, pp. 1-41.
- Occhipinti, S.A., Reddy, S.M., 2009. Neoproterozoic reworking of the Palaeoproterozoic Capricorn Orogen of Western Australia and implications for the amalgamation of Rodinia. *Geological Society, London, Special Publications* 327, 445-456.
- Occhipinti, S.A., Sheppard, S., Passchier, C., Tyler, I.M., Nelson, D.R., 2004. Palaeoproterozoic crustal accretion and collision in the southern Capricorn Orogen: the Glenburgh Orogeny. *Precambrian Research* 128, 237-255.
- Olierook, H.K.H., Agangi, A., Plavsa, D., Reddy, S.M., Clark, C., Yao, W.-H., Occhipinti, S.A., Kylander-Clark, A.R.C., in review. Neoproterozoic hydrothermal activity in the West Australian Craton related to Rodinia assembly or breakup? *Earth and Planetary Science Letters*.
- Paton, C., Hellstrom, J., Paul, B., Woodhead, J., Hergt, J., 2011. Iolite: Freeware for the visualisation and processing of mass spectrometric data. *Journal of Analytical Atomic Spectrometry* 26, 2508-2518.
- Piccoli, P., Candela, P., Rivers, M., 2000. Interpreting magmatic processes from accessory phases: titanite—a small-scale recorder of large-scale processes. *Earth and Environmental Science Transactions of the Royal Society of Edinburgh* 91, 257-267.

- Pidgeon, R.T., Bosch, D., Bruguier, O., 1996. Inherited zircon and titanite U–Pb systems in an Archaean syenite from southwestern Australia: implications for U–Pb stability of titanite. *Earth and Planetary Science Letters* 141, 187-198.
- Piechocka, A.M., Gregory, C.J., Zi, J.-W., Sheppard, S., Wingate, M.T.D., Rasmussen, B., 2017. Monazite trumps zircon: applying SHRIMP U–Pb geochronology to systematically evaluate emplacement ages of leucocratic, low-temperature granites in a complex Precambrian orogen. *Contributions to Mineralogy and Petrology* 172, 63.
- Piechocka, A.M., Sheppard, S., Fitzsimons, I.C.W., Johnson, S.P., Rasmussen, B., Jourdan, F., 2018. Neoproterozoic $^{40}\text{Ar}/^{39}\text{Ar}$ mica ages mark the termination of a billion years of intraplate reworking in the Capricorn Orogen, Western Australia. *Precambrian Research* 310, 391-406.
- Plavsa, D., Reddy, S., Clark, C., Agangi, A., 2018. Capricorn Orogen regional rutile study: a combined EBSD and Laser- Ablation Split-Stream (LASS) analytical approach. Geological Survey of Western Australia, Record 2018/15.
- Prowatke, S., Klemme, S., 2005. Effect of melt composition on the partitioning of trace elements between titanite and silicate melt. *Geochimica et Cosmochimica Acta* 69, 695-709.
- Rasmussen, B., Fletcher, I.R., Muhling, J.R., 2013. Dating deposition and low-grade metamorphism by in situ UPb geochronology of titanite in the Paleoproterozoic Timeball Hill Formation, southern Africa. *Chemical Geology* 351, 29-39.

- Rasmussen, B., Fletcher, I.R., Sheppard, S., 2005. Isotopic dating of the migration of a low-grade metamorphic front during orogenesis. *Geology* 33, 773-776.
- Rubatto, D., Williams, I.S., Buick, I.S., 2001. Zircon and monazite response to prograde metamorphism in the Reynolds Range, central Australia. *Contributions to Mineralogy and Petrology* 140, 458-468.
- Scott, D.J., St-Onge, M.R., 1995. Constraints on Pb closure temperature in titanite based on rocks from the Ungava orogen, Canada: Implications for U-Pb geochronology and P-T-t path determinations. *Geology* 23, 1123-1126.
- Shannon, R.D., 1976. Revised effective ionic radii and systematic studies of interatomic distances in halides and chalcogenides. *Acta crystallographica section A: crystal physics, diffraction, theoretical and general crystallography* 32, 751-767.
- Sheppard, S., Bodorkos, S., Johnson, S.P., Wingate, M.T.D., Kirkland, C.L., 2010a. The Paleoproterozoic Capricorn Orogeny: Intracontinental reworking not continent-continent collision. *Geological Survey of Western Australia, Report 108*, 33p.
- Sheppard, S., Johnson, S.P., Wingate, M.T.D., Kirkland, C.L., Pirajno, F., 2010b. Explanatory notes for the Gascoyne Province. *Geological Survey of Western Australia, Perth, Western Australia*.
- Sheppard, S., Occhipinti, S.A., Nelson, D.R., 2005. Intracontinental reworking in the Capricorn Orogen, Western Australia: the 1680–1620 Ma Gascoyne Orogeny. *Australian Journal of Earth Sciences* 52, 443-460.

- Sheppard, S., Occhipinti, S.A., Tyler, I.M., 2004. A 2005–1970 Ma Andean-type batholith in the southern Gascoyne Complex, Western Australia. *Precambrian Research* 128, 257-277.
- Sheppard, S., Rasmussen, B., Muhling, J.R., Farrell, T.R., Fletcher, I.R., 2007. Grenvillian-aged orogenesis in the Palaeoproterozoic Gascoyne Complex, Western Australia: 1030–950 Ma reworking of the Proterozoic Capricorn Orogen. *Journal of Metamorphic Geology* 25, 477-494.
- Simonetti, A., Heaman, L.M., Chacko, T., Banerjee, N.R., 2006. In situ petrographic thin section U–Pb dating of zircon, monazite, and titanite using laser ablation–MC–ICP–MS. *International Journal of Mass Spectrometry* 253, 87-97.
- Spandler, C., Hammerli, J., Sha, P., Hilbert-Wolf, H., Hu, Y., Roberts, E., Schmitz, M., 2016. MKED1: A new titanite standard for in situ analysis of Sm–Nd isotopes and U–Pb geochronology. *Chemical Geology* 425, 110-126.
- Spencer, C.J., Kirkland, C.L., Taylor, R.J.M., 2016. Strategies towards statistically robust interpretations of in situ U–Pb zircon geochronology. *Geoscience Frontiers* 7, 581-589.
- Spencer, K.J., Hacker, B.R., Kylander-Clark, A.R.C., Andersen, T.B., Cottle, J.M., Stearns, M.A., Poletti, J.E., Seward, G.G.E., 2013. Campaign-style titanite U–Pb dating by laser-ablation ICP: Implications for crustal flow, phase transformations and titanite closure. *Chemical Geology* 341, 84-101.

- Stacey, J.S., Kramers, J.D., 1975. Approximation of terrestrial lead isotope evolution by a two-stage model. *Earth and Planetary Science Letters* 26, 207-221.
- Sun, S.-s., McDonough, W.F., 1989. Chemical and isotopic systematics of oceanic basalts: implications for mantle composition and processes. Geological Society, London, Special Publications 42, 313-345.
- Taylor, R.J.M., Clark, C., Fitzsimons, I.C.W., Santosh, M., Hand, M., Evans, N., McDonald, B., 2014. Post-peak, fluid-mediated modification of granulite facies zircon and monazite in the Trivandrum Block, southern India. *Contributions to Mineralogy and Petrology* 168, 1044.
- Tera, F., Wasserburg, G.J., 1972. U-Th-Pb systematics in three Apollo 14 basalts and the problem of initial Pb in lunar rocks. *Earth and Planetary Science Letters* 14, 281-304.
- Tiepolo, M., Oberti, R., Vannucci, R., 2002. Trace-element incorporation in titanite: constraints from experimentally determined solid/liquid partition coefficients. *Chemical Geology* 191, 105-119.
- Timms, N.E., Kinny, P.D., Reddy, S.M., Evans, K., Clark, C., Healy, D., 2011. Relationship among titanium, rare earth elements, U-Pb ages and deformation microstructures in zircon: Implications for Ti-in-zircon thermometry. *Chemical Geology* 280, 33-46.
- Tomkins, H.S., Powell, R., Ellis, D.J., 2007. The pressure dependence of the zirconium-in-rutile thermometer. *Journal of Metamorphic Geology* 25, 703-713.

- Tyler, I., 1991. The geology of the Sylvania Inlier and the southeast Hamersley Basin. Geological Survey of Western Australia.
- Verts, L.A., Chamberlain, K.R., Frost, C.D., 1996. U-Pb sphene dating of metamorphism: the importance of sphene growth in the contact aureole of the Red Mountain pluton, Laramie Mountains, Wyoming. *Contributions to Mineralogy and Petrology* 125, 186-199.
- Watson, E.B., Wark, D.A., Thomas, J.B., 2006. Crystallization thermometers for zircon and rutile. *Contributions to Mineralogy and Petrology* 151, 413.
- Wingate, M.T.D., Giddings, J.W., 2000. Age and palaeomagnetism of the Mundine Well dyke swarm, Western Australia: implications for an Australia–Laurentia connection at 755 Ma. *Precambrian Research* 100, 335-357.
- Wingate, M.T.D., Kirkland, C.L., Bodorkos, S., Sheppard, S., 2009a. 180938: monzogranite, Leake Spring: Geochronology Record 751. Geological Survey of Western Australia, pp. 1-4.
- Wingate, M.T.D., Kirkland, C.L., Bodorkos, S., Sheppard, S., Farrell, T.R., 2009b. 183215: porphyritic metamonzogranite, Davey Well; Geochronology Record 771. Geological Survey of Western Australia, pp. 1-4.
- Wingate, M.T.D., Kirkland, C.L., Johnson, S.P., 2013a. 195819: metamonzogranite, Bee Well Creek; Geochronology Record 1098. Geological Survey of Western Australia, pp. 1-4.

- Wingate, M.T.D., Kirkland, C.L., Johnson, S.P., 2013b. 195821: metagranodiorite, Wirradong Well; Geochronology Record 1100. Geological Survey of Western Australia, pp. 1-4.
- Wingate, M.T.D., Kirkland, C.L., Johnson, S.P., 2013c. 195826: monzogranitic gneiss, McCarthy Well; Geochronology Record 1104. Geological Survey of Western Australia, pp. 1-5.
- Wingate, M.T.D., Kirkland, C.L., Johnson, S.P., Sheppard, S., 2012. 190661: metatonalite, Midway Bore; Geochronology Record 1037. Geological Survey of Western Australia, pp. 1-4.
- Wingate, M.T.D., Kirkland, C.L., Thorne, A.M., Johnson, S.P., 2014. 169885: biotite granodiorite, Stuarts Well; Geochronology Record 1208. Geological Survey of Western Australia, pp. 1-4.
- Zack, T., Moraes, R., Kronz, A., 2004. Temperature dependence of Zr in rutile: empirical calibration of a rutile thermometer. *Contributions to Mineralogy and Petrology* 148, 471-488.
- Zhang, S.-B., Zheng, Y.-F., Wu, Y.-B., Zhao, Z.-F., Gao, S., Wu, F.-Y., 2006. Zircon U-Pb age and Hf-O isotope evidence for Paleoproterozoic metamorphic event in South China. *Precambrian Research* 151, 265-288.

Figure Captions

Fig. 1: Geological map of the main tectonic units in the Capricorn Orogen, Western Australia, showing titanite and zircon samples used in this paper, and major mineral deposits from Geoview (<https://geoview.dmp.wa.gov.au>). Note that iron and manganese ore deposits are not shown.

Fig. 2: Detailed geological map of the western Capricorn Orogen (Gascoyne Province), modified from Plavsa et al. (2018).

Fig. 3: Representative BSE images of titanite morphology, zoning patterns, inclusions and adjacent minerals. For representative BSE images from each sample, see supplementary material. ttn = titanite

Fig. 4: Examples of Tera-Wasserburg inverse concordia plot for titanite samples that record a single age. (a) Partially concordant data from porphyritic monzogranite sample 88414, calculated using lower concordia intercept. (b) Wholly discordant data from felsic intrusion sample 190661, calculated using lower discordia intercept. (c) Proterozoic granodiorite sample 195821 with more Pb associated with higher discordance, interpreted as more common Pb incorporation. Age calculated using weighted mean of uncorrected $^{206}\text{Pb}/^{238}\text{U}$ dates with $f_{207} < 1\%$. (d) Archean granitic sample 84557 with possible multiple common-Pb reservoirs but converging to single concordant age, calculated using weighted mean of

Page 50

uncorrected $^{206}\text{Pb}/^{238}\text{U}$ dates with $f_{207} < 1\%$. Analysis colors correspond to the two groups defined by different REE gradients in the inset, showing no systematic difference in age between the two chemical groups.

Fig. 5: Examples of Tera-Wasserburg inverse concordia plot for titanite samples that record two ages. (a) Granite sample 120644 showing high Zr- and Pb-bearing titanite for grains older than ca. 2700 Ma with variable incorporation of common Pb and low Zr- and Pb-bearing titanite spread between ca. 2700 Ma and 1800 Ma, indicative of metamorphic recrystallization, Zr-loss and Pb-loss of originally igneous grains. (b) Monzogranite sample 84599 show a triangular wedge of U–Pb data between a single $^{207}\text{Pb}/^{206}\text{Pb}$ and two points on the concordia curve with systematic differences in Th/U ratios; (c) Granite sample 195826 showing U–Pb data spread along the concordia as well as up and right into discordia space.

Fig. 6: Comparison of statistically reliable weighted zircon and titanite ages (Table 2). (a) Archean terranes. (b) Coeval to slight temporal differences from the Moorarie and Durlacher Supersuites. (c) Significant temporal differences between zircon and titanite related to known tectonothermal events. U–Pb ages are uncorrected $^{207}\text{Pb}/^{206}\text{Pb} > 1.5$ Ga and $^{206}\text{Pb}/^{238}\text{U}$ for zircon, and $^{206}\text{Pb}/^{238}\text{U} < 2.0$ Ga for titanite. Zircon U–Pb data is publicly available (Bodorkos et al., 2006a, b, c; Bodorkos et al., 2006d, e, f, g; Jahn, in review; Nelson, 2004, 2005; Wingate et al., 2009a; Wingate et al., 2009b; Wingate et al., 2013a, b, c; Wingate et al., 2012; Wingate et al., 2014).

Fig. 7: Titanite trace element discrimination indices. Data are color-coded by neocrystallized igneous grains (igneous), recrystallized igneous grains (recryst.) or neocrystallized metamorphic grains (meta./metamorphic).

Fig. 8: Trace element ratios (a) $(\text{La}/\text{Sm})_{\text{N}}$, and (b) $(\text{Eu}/\text{Eu}^*)_{\text{N}}$ vs. apparent U–Pb ages from the Moorarie and Durlacher Supersuites. The symbol shape (circle, square, rectangle) defined in panels (a) and (d) also applies to panels (c), (d) and (e), (f), respectively.

Fig. 9: Kriging plots of single neocrystallized igneous and recrystallized igneous titanite grains. (a) neocrystallized igneous titanite from sample 88414 of the Moorarie Supersuite and exhibiting an apparent $^{206}\text{Pb}/^{238}\text{U}$ age increase from core to rim, color-coded by apparent $^{206}\text{Pb}/^{238}\text{U}$ date. However, this reflects an increase in common-Pb during crystallisation, as revealed by the Tera-Wasserburg concordia diagram, and the color-coded discordance plot. There is close agreement between the zonation patterns of La/Sm and Eu/Eu* ratios, showing concentric zonation consistent with the original igneous crystallisation. (b) recrystallized igneous titanite from sample 195826 of the Durlacher Supersuite, exhibiting Mesoproterozoic Pb-loss increasing from the grains interior towards exterior, color-coded by apparent $^{206}\text{Pb}/^{238}\text{U}$ date. The apparent $^{206}\text{Pb}/^{238}\text{U}$ ages for eight analyses across the grain and the Tera-Wasserburg concordia diagram highlight the intra-grain Pb-loss trajectory towards 1200 Ma, consistent with metamorphic zircon ages (1200 ± 3 Ma; Wingate et al., 2013c). The more discordant analyses correlate with regions of the grain that either contained inherited common-Pb or where recrystallization has resulted in increased incorporation of common-Pb.

The behaviour of the trace elements was variable during recrystallization. La/Sm exhibits a concentric zonation pattern, while Eu/Eu* appears to more closely correlate with domains of recrystallization.

Fig. 10: Principal component (PC) analysis summary showing PC scores for individual spot analyses and PC loadings for individual element variables. Plotted data are differentiated by (a) igneous, recrystallized and neocrystallized titanite, and (b) tectonic suite. Compositional biplots showing principal component scores for individual titanite spot analyses and PC loadings for the different trace element variables. For both (a) and (b), left and bottom axes correspond to colored dots, whereas right and top axes correspond to gray circles with various element labels.

Fig. 11: Schematic Tera-Wasserburg diagram for interpreting common-Pb, crystallization and recrystallization mixing lines from titanite data. While U–Pb data from common-Pb bearing phases may appear complex, especially in scenarios that involve recrystallization, the spread of data simply shows an array/mixing line between a common-Pb, and a radiogenic Pb components (red arrow). During recrystallization, this pattern is further complicated by moving any previous U–Pb/Pb–Pb ratios towards a new mixing line between common-Pb and the new radiogenic age (pale, dashed blue line). Depending on the incorporation of common-Pb at this time a variety of data trends may be seen (bold blue lines). The result may require careful interpretation with little concordant data.

Fig. 12: Inverse distance weighted surface of U–Pb ages from titanite across the Capricorn Orogen (grey dots) with major tectonic lineaments demarked. Interpolation is stretched at a 2:1 ratio at a strike of 110° based on the general structural trend of the orogen, smoothed at 0.4, and each individual point weighted by the reciprocal of their uncertainty. If igneous and metamorphic events are recorded in a single sample, the youngest titanite age is used.

Table 1: Summary of sample location, titanite ages and zircon ages. Coordinates are in WGS 1984.

Table 2: Titanite and zircon ages for the same samples. Zircon U–Pb data is publicly available (Bodorkos et al., 2006a, b, c; Bodorkos et al., 2006d, e, f, g; Jahn, in review; Nelson, 2004, 2005; Wingate et al., 2009a; Wingate et al., 2009b; Wingate et al., 2013a, b, c; Wingate et al., 2012; Wingate et al., 2014).

Supplementary Table A: Trace element data for the Khan titanite reference material.

Supplementary Table B: Compendium of all analytical data for titanite data.

Table 1

Sample	Lithology	Suite *	Formation	Lat.	Long.	Age (Ma \pm 2 σ)	<i>n</i>	MSWD	<i>p</i>	²⁰⁷ Pb/ ²⁰⁶ Pb intercept
81867	Monzogranite	1	Sylvania Inlier	-23.72	119.77	**I: 3170 \pm 58	5 of 23	1.90	0.10	0.95 \pm 0.36
84557	Granite	1	Sylvania Inlier	-23.49	119.50	**I: 2938 \pm 14	15 of 51	1.5	0.10	0.49 \pm 0.03
84599	Monzogranite	1	Sylvania Inlier	-23.38	119.97	***I: 2937 \pm 67	13 of 98	1.40	0.15	0.83 \pm 0.01
81886	Recrystallized Granite	1	Sylvania Inlier	-23.72	119.92	<i>Insufficient data</i>				
80434	Granodiorite	2	Narryer Terr.	-25.77	117.48	<i>No reliable age (~Mesoarchean)</i>				
152855	Granite	2	Kalgoorlie Terr.	-25.91	120.43	**I: 2672 \pm 22	8 of 37	1.07	0.38	0.63 \pm 0.03
135469	Foliated Amphibolite	2	Yarlarweelor	-25.36	117.56	<i>No reliable age (~Mesoproterozoic)</i>				
80491	Biotite Monzogranite	2	Yarlarweelor	-25.48	118.26	<i>Insufficient data</i>				
120700	Granodiorite	2	Marymia Inlier	-25.57	119.01	***I: 2666 \pm 22	5 of 46	0.7	0.57	1.07 \pm 0.11
JCO15/1	Granite	2	Marymia Inlier	-25.48	119.47	<i>Insufficient data</i>				
120644	Granite	2	Goodin Inlier	-25.97	119.20	**I: 2644 \pm 17	12 of 40	1.2	0.28	0.55 \pm 0.03
						M: 1850 \pm 120	6 of 6	1.30	0.31	0.31 \pm 0.05
120649	Granite	2	Goodin Inlier	-25.99	119.16	<i>No reliable age (~Paleoproterozoic)</i>				
120678	Granite	2	Goodin Inlier	-25.79	119.43	<i>Insufficient data</i>				
142925	Biotite Monzogranite	3	Dalgaringa SS	-25.31	116.41	<i>No reliable age</i>				

142926	Foliated Biotite Tonalite	3	Dalgaringa SS	-25.32	116.44					<i>No reliable age</i>
142928	Biotite Tonalite	3	Nardoo Granite	-25.44	116.45					<i>No reliable age</i>
135501	Granodiorite	3	Bertibubba SS	-25.33	117.56					<i>No reliable age (~Mesoproterozoic)</i>
135497	Foliated Granite	3	Bertibubba SS	-25.36	117.56					<i>Insufficient data</i>
195821	Granodiorite	4	Moorarie SS	-23.88	115.31	**I: 1808 ± 11	16 of 50	0.30	1.00	0.78 ± 0.04
88411	Biotite Monzogranite	4	Minnie Creek	-24.12	115.94	I: 1801 ± 14	38 of 43	0.90	0.65	0.87 ± 0.18
JCO14/ 4-09	Biotite Granite	4	Moorarie SS	-24.08	115.87	**I: 1789 ± 10	16 of 39	0.82	0.65	1.05 ± 0.26
178024	Biotite Granodiorite	4	Minnie Creek	-23.95	115.53	I: 1786 ± 17	30 of 30	1.03	0.42	0.71 ± 0.11
88407	Porphyritic Monzogranite	4	Minnie Creek	-24.16	116.15	I: 1785 ± 7	58 of 58	1.3	0.07	1.19 ± 0.27
169885	Biotite Granodiorite	4	Moorarie SS	-24.07	115.67	I: 1780 ± 14	12 of 12	1.6	0.10	0.81 ± 0.10
88405	Biotite Granodiorite	4	Minnie Creek	-24.22	116.19	**I: 1776 ± 11	24 of 45	0.87	0.64	0.40 ± 0.04
88415	Porphyritic Granodiorite Dyke	4	Minnie Creek	-24.07	115.67	I: 1763 ± 15	45 of 45	0.75	0.89	0.82 ± 0.15
88414	Porphyritic Monzogranite	4	Minnie Creek	-24.07	115.67	I: 1757 ± 11	46 of 46	0.96	0.55	0.79 ± 0.12
88412	Foliated Porphyritic Monzogranite	4	Minnie Creek	-24.12	115.92	†I: 1753 ± 12	36 of 41	0.49	1.00	-
135433	Granitic Gneiss	4	Moorarie SS	-25.39	117.88					<i>No reliable age (~Paleo/Mesoproterozoic)</i>
190661	Porphyritic Granite	4	Moorarie SS	-24.59	116.65	M: 1248 ± 67	43 of 44	1.20	0.19	1.04 ± 0.13
190660	Biotite Monzogranite	4	Moorarie SS	-24.59	116.65					<i>No reliable age (~Mesoproterozoic)</i>
88420	Biotite Granodiorite	4	Minnie Creek	-24.24	115.82	M: 1170 ± 15	48 of 48	0.91	0.65	0.79 ± 0.11
142924	Biotite-Muscovite Granodiorite	4	Moorarie SS	-25.27	116.44	M: 863 ± 65	36 of 36	0.98	0.51	0.79 ± 0.02

180938	Monzogranite	4	Moorarie SS	-24.44	116.57					<i>No reliable age</i>
195825	Biotite Granodiorite	4	Moorarie SS	-24.18	115.38					<i>Insufficient data</i>
JCO14/ 4-04	Leucocratic Granite	4	Moorarie SS	-23.86	115.75					<i>Insufficient data</i>
143546	Porphyritic Granite	4	Moorarie SS	-25.62	117.75					<i>Insufficient data</i>
183215	Porphyritic Monzogranite	5	Durlacher SS	-24.39	115.90	**I: 1646 ± 12	24 of 46	0.94	0.54	0.61 ± 0.29
195826	Granite	5	Davey Well	-24.56	115.74	***I: 1698 ± 130	13 of 46	1.7	0.07	0.15 ± 0.01
						***M: 1033 ± 90	13 of 46			
195819	Monzogranite	5	Durlacher SS	-23.83	115.33	M: 1110 ± 54	7 of 9	0.85	0.51	0.59 ± 0.02
169090	Porphyritic Biotite Monzogranite	5	Durlacher SS	-23.39	115.53	M: 959 ± 88	32 of 34	1.4	0.06	0.69 ± 0.03
DW14/ 7-07	Gneiss	5	Davey Well Batholith	-24.77	116.01					<i>No reliable age</i>
169092	Biotite-Muscovite Monzogranite	5	Durlacher SS	-23.42	115.64					<i>Insufficient data</i>

* 1: Pilbara Craton; 2: Yilgarn Craton; 3: Glenburgh Orogeny; 4: Capricorn Orogeny; 5: Mangaroon Orogeny.

** Statistically-inconsistent $^{207}\text{Pb}/^{206}\text{Pb}$ intercept; age calculated via $f_{207} < 1\%$ only.

*** Age calculated based on data that are differentiated on chemical criteria

† No ^{207}Pb -correction, >85% data concordant; uncorrected concordant dates used for age calculation.

Note: Latitude and longitude are in WGS 84.

Table 2

Sample	Suite *	Formation	Titanite Age		Zircon ²⁰⁷ Pb/ ²⁰⁶ Pb Age			
81867	1	Sylvania Inlier	I: 3170 ± 58	I: 3187 ± 50	3 of 3	1.4	0.25	Jahn (in review)
84599	1	Sylvania Inlier	I: 2937 ± 67	I: 2924 ± 14	3 of 3	0.53	0.59	Jahn (in review)
152855	2	Kalgoorlie Terr.	I: 2672 ± 22	No reliable age (ca. 2.65 Ma)				Jahn (in review)
120644	2	Goodin Inlier	I: 2644 ± 17 M: 50 ± 120	I: 2641 ± 15	5 of 5	0.94	0.44	Jahn (in review)
195821	4	Moorarie SS	I: 1808 ± 11	I: 1793 ± 6	15 of 15	0.94	0.52	Wingate et al. (2013b)
88411	4	Minnie Creek	I: 1801 ± 14	I: 1791 ± 9	21 of 21	0.85	0.65	Bodorkos et al. (2006a)
JCO14/ 09	4-	Moorarie SS	I: 1789 ± 10	I: 1813 ± 5	17 of 17	0.74	0.76	Jahn (in review)
178024	4	Minnie Creek	I: 1786 ± 17	I: 1783 ± 5	26 of 26	0.88	0.64	Nelson (2005)
88407	4	Minnie Creek	I: 1785 ± 7	I: 1795 ± 7	30 of 30	1.5	0.05	Bodorkos et al. (2006e)
169885	4	Moorarie SS	I: 1780 ± 14	I: 1796 ± 9	20 of 20	0.41	0.99	Wingate et al. (2014)
88405	4	Minnie Creek	I: 1776 ± 11	I: 1792 ± 5	41 of 41	1.4	0.05	Bodorkos et al. (2006d)
88415	4	Minnie Creek	I: 1763 ± 15	I: 1777 ± 8	13 of 13	1.13	0.33	Bodorkos et al. (2006c)
88414	4	Minnie Creek	I: 1757 ± 11	I: 1783 ± 5	19 of 19	1.0	0.46	Bodorkos et al. (2006b)
88412	4	Minnie Creek	I: 1753 ± 12	I: 1798 ± 5	28 of 28	1.2	0.19	Bodorkos et al. (2006f)

190661	4	Moorarie SS	M: 1248 ± 67	I: 1800 ± 5	8 of 8	1.10	0.36	Wingate et al. (2012)
88420	4	Minnie Creek	M: 1170 ± 15	I: 1787 ± 5	35 of 35	2.1	0.00	Bodorkos et al. (2006g)
142924	4	Moorarie SS	M: 863 ± 65	I: 1783 ± 5	21 of 21	1.3	0.15	Wingate et al. (2009a)
183215	5	Durlacher SS	I: 1646 ± 12	I: 1664 ± 5	25 of 25	0.54	0.97	Wingate et al. (2009b)
195826	5	Davey Well	I: 1698 ± 130	I: 1664 ± 6	12 of 12	1.4	0.17	Wingate et al. (2013c)
			M: 1033 ± 90	M: 1195 ± 14	5 of 5	0.23	0.92	
195819	5	Durlacher SS	M: 1110 ± 54	I: 1666 ± 9	12 of 12	0.50	0.91	Wingate et al. (2013a)
169090	5	Durlacher SS	M: 959 ± 88	I: 1691 ± 13	4 of 4	2.0	0.11	Nelson (2004)

* 1: Pilbara Craton; 2: Yilgarn Craton; 3: Glenburgh Orogeny; 4: Capricorn Orogeny; 5: Mangaroon Orogeny

Highlights

- Workflow presented for robust interpretation of titanite U–Pb and trace element data
- Trace element data effective at differentiating igneous, recrystallized and metamorphic titanite
- Differentiation indices include Zr-in-titanite T, Th/U, Th/Pb, Al/(Al+Fe), REE ratios and Eu/Eu*
- Titanite provides better understanding of late-stage tectonothermal events complex terranes

ACCEPTED MANUSCRIPT

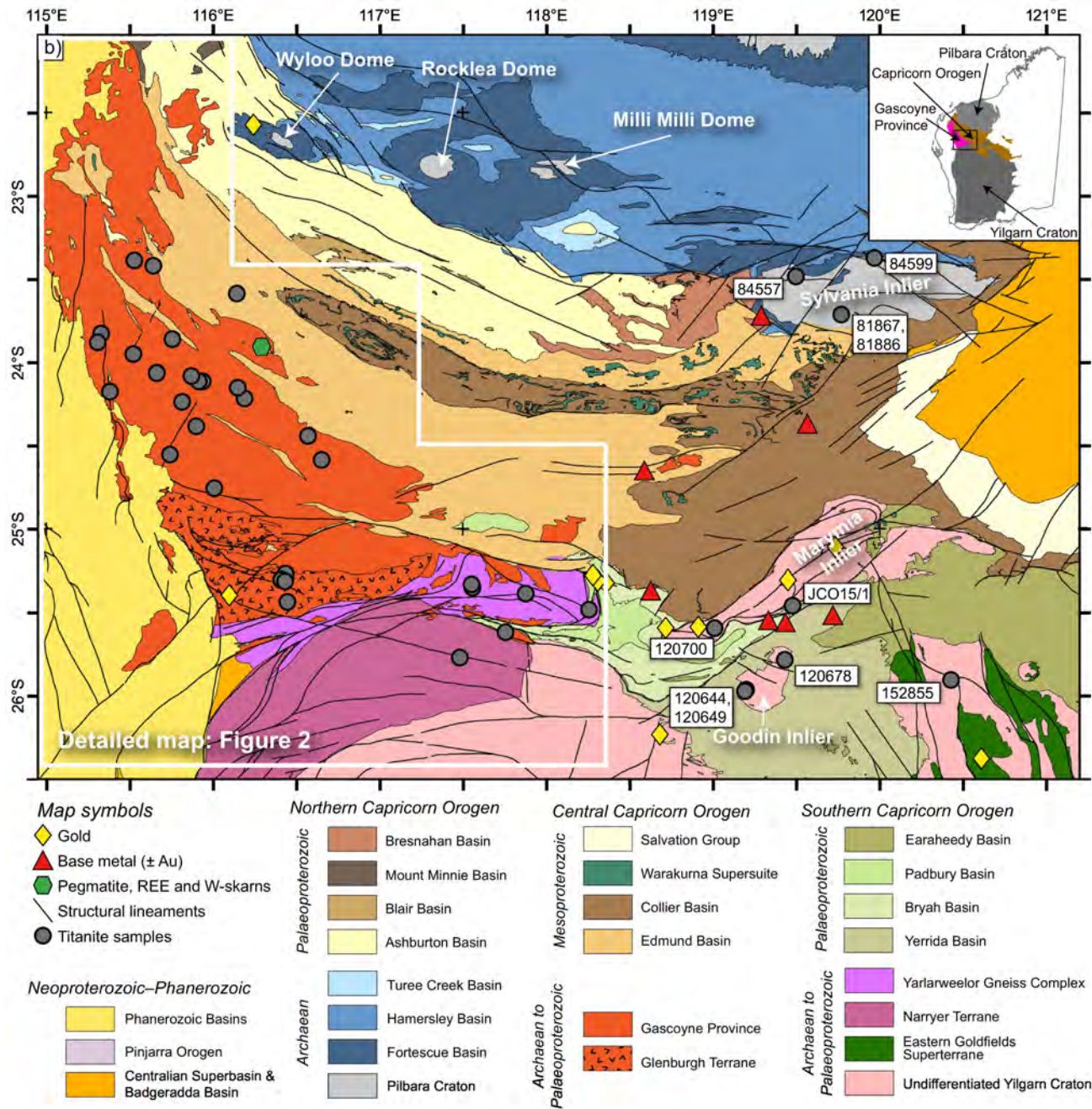


Figure 1

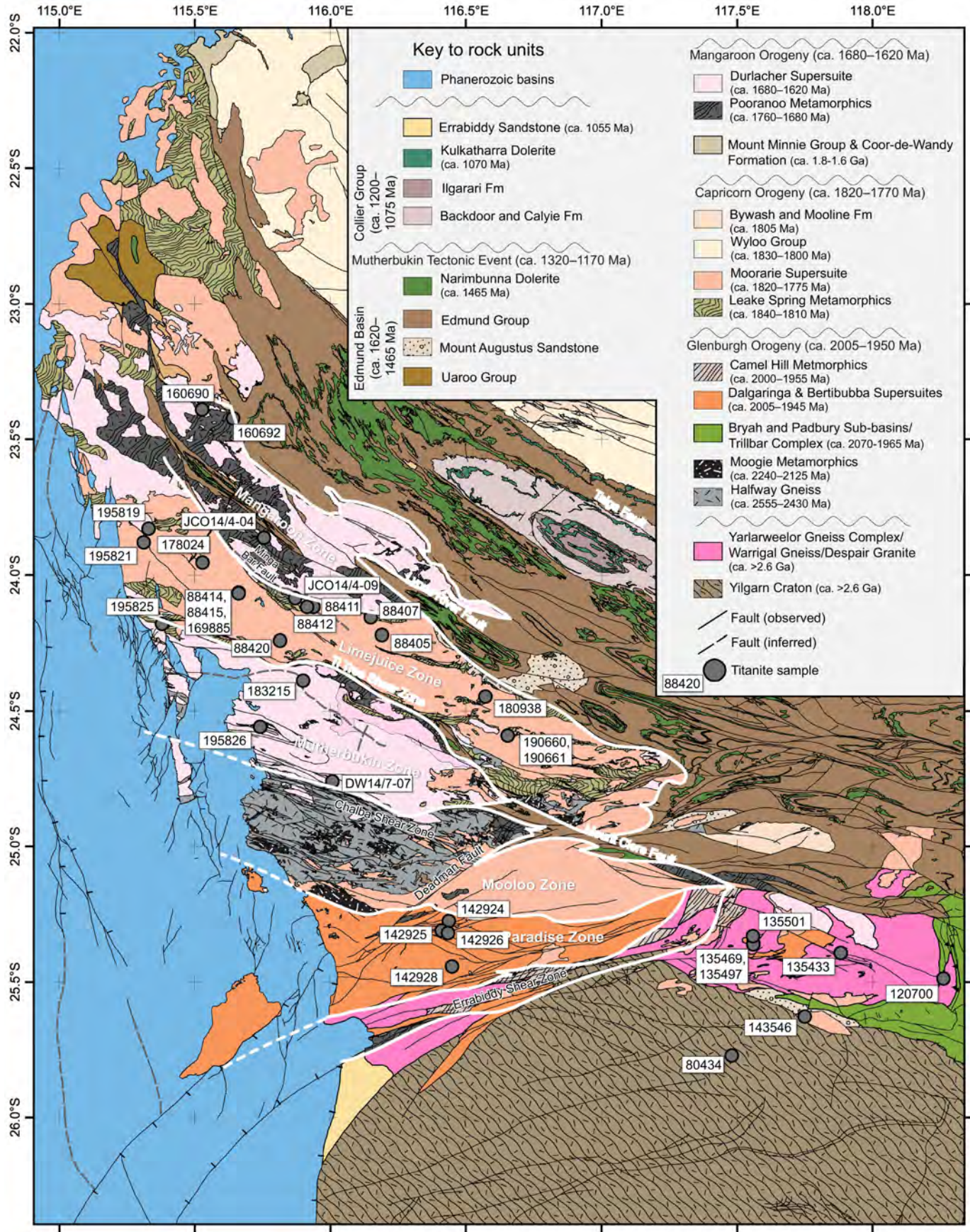
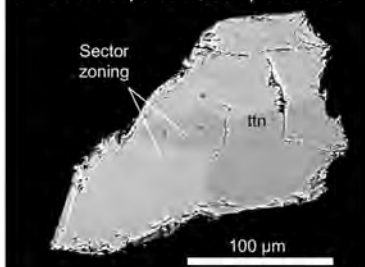


Figure 2

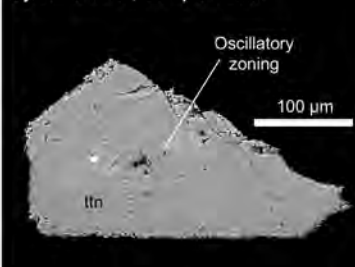
a Igneous, sector zoning

Durlacher Supersuite, Sample 183215



b Igneous, oscillatory zoning

Sylvania Inlier, Sample 84557



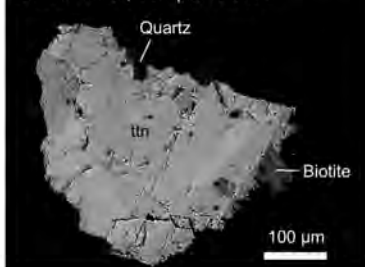
c Igneous, BSE-homogenous

Moorarie Supersuite, Sample 195821



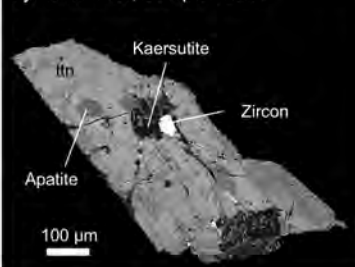
d Igneous, 'sugary' alteration

Goodin Inlier, Sample 120644



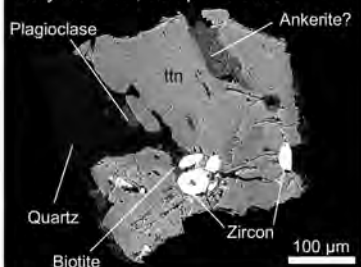
e Igneous, zircon/apatite inclusions

Sylvania Inlier, Sample 84557



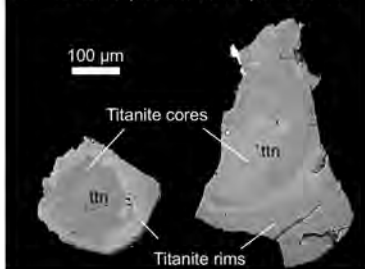
f Igneous, zircon inclusions

Marymia Inlier, Sample 120700



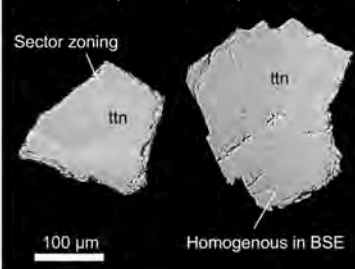
g Recrystallized titanite

Durlacher Supersuite, Sample 195826



h Metamorphic, two textures

Moorarie Supersuite, Sample 88420



i Metamorphic, ilmenite inclusions

Durlacher Supersuite, Sample 195819

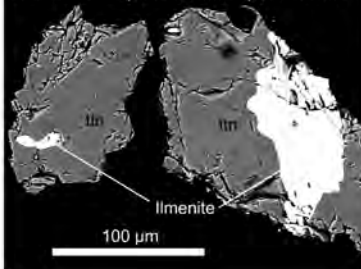


Figure 3

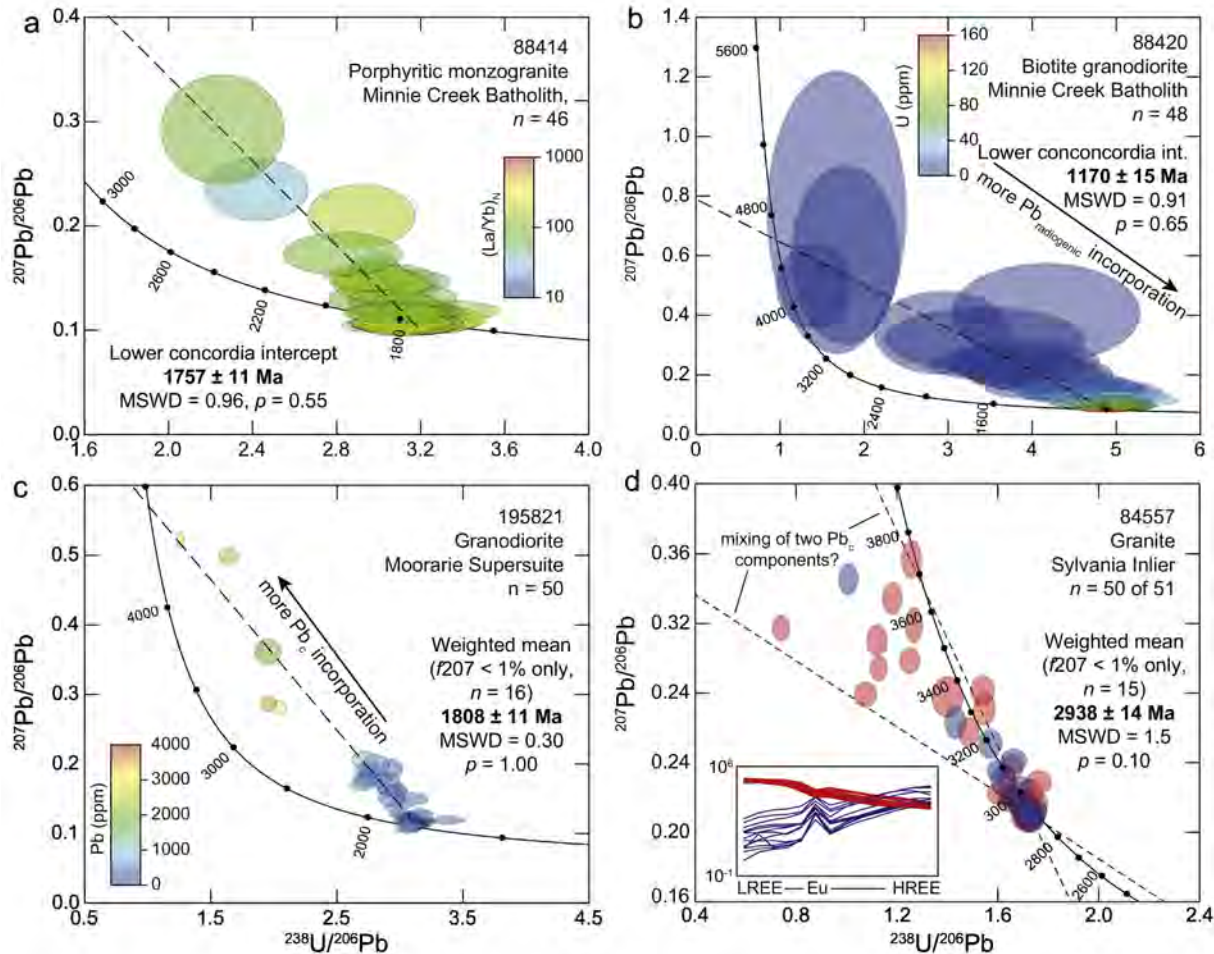


Figure 4

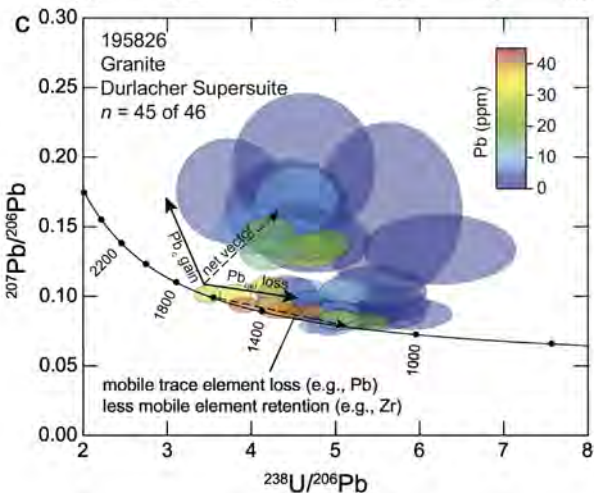
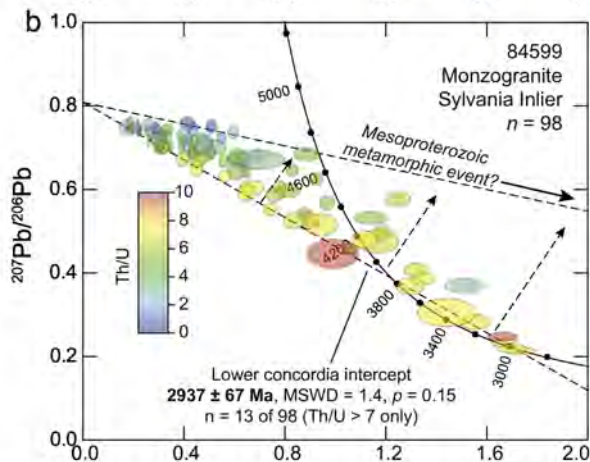
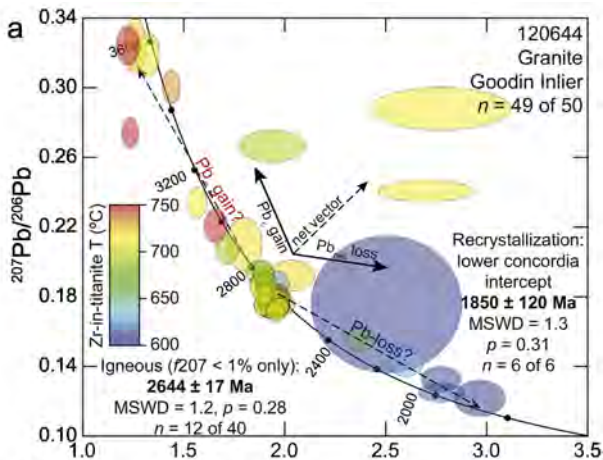


Figure 5

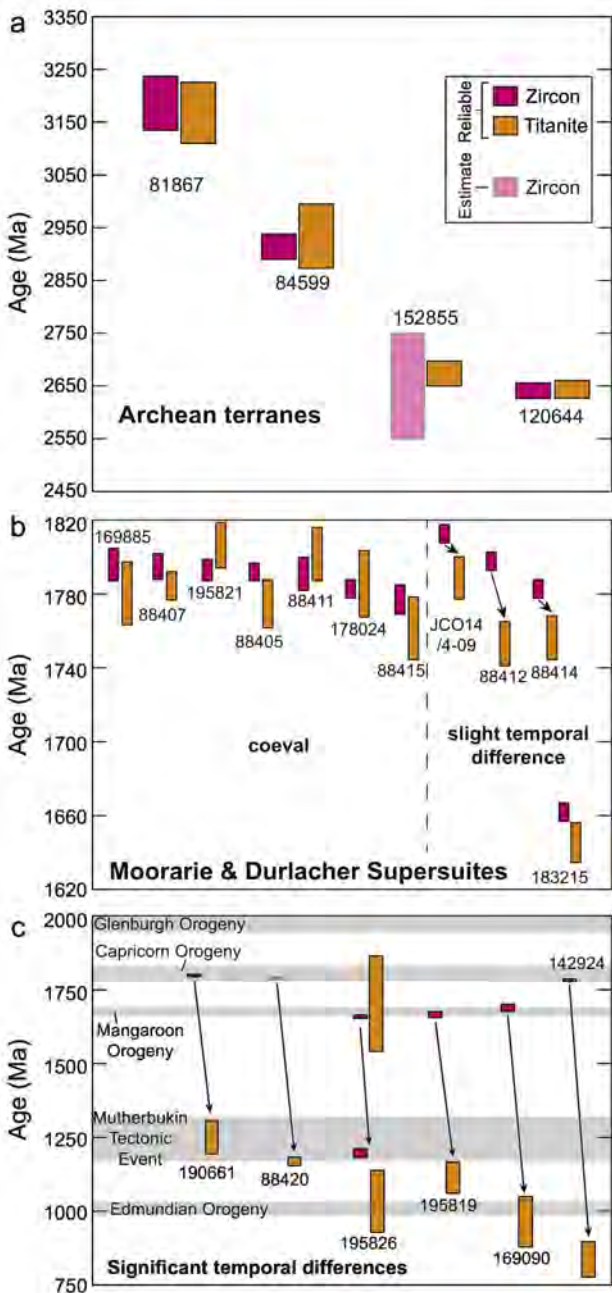


Figure 6

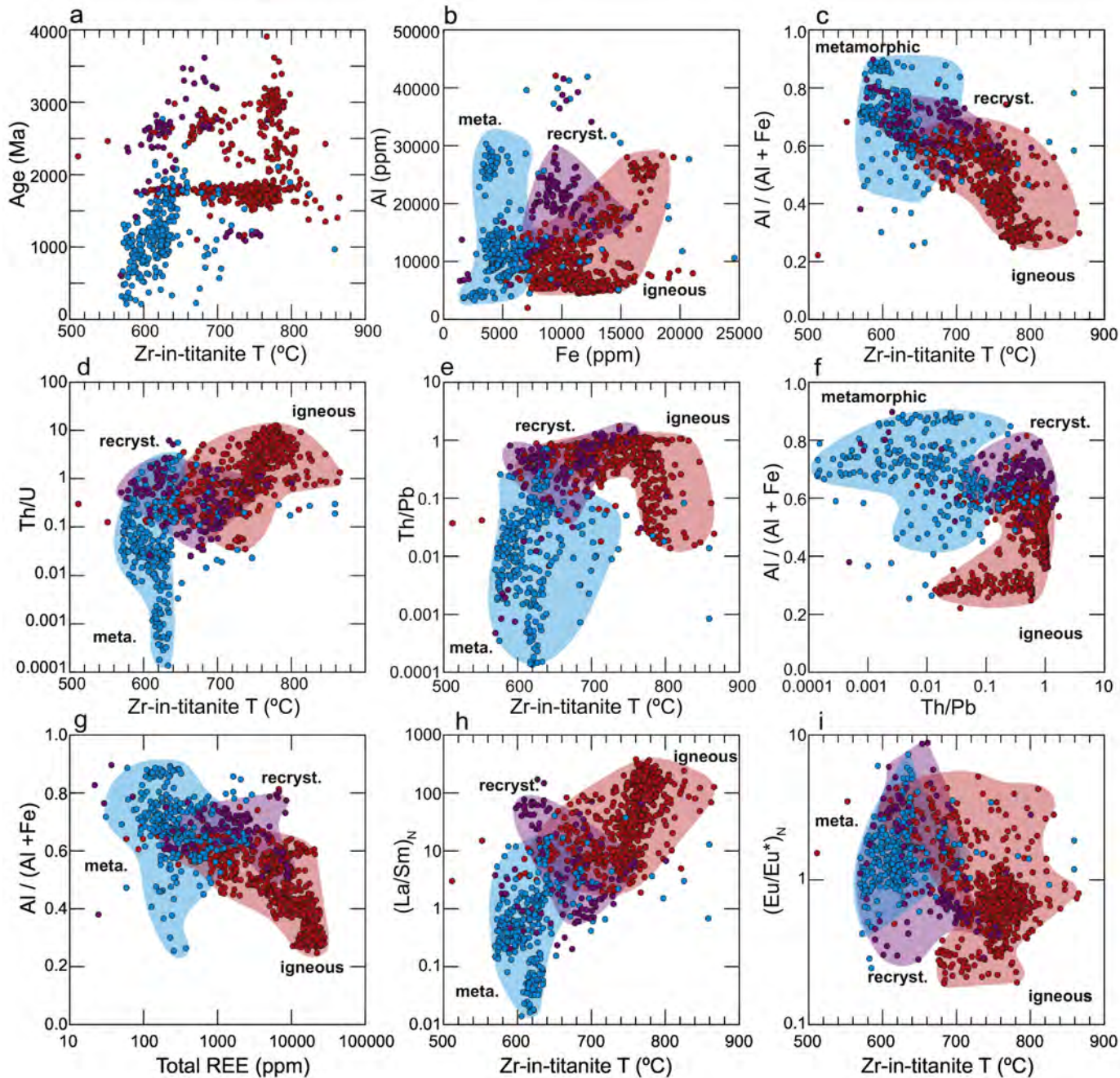


Figure 7

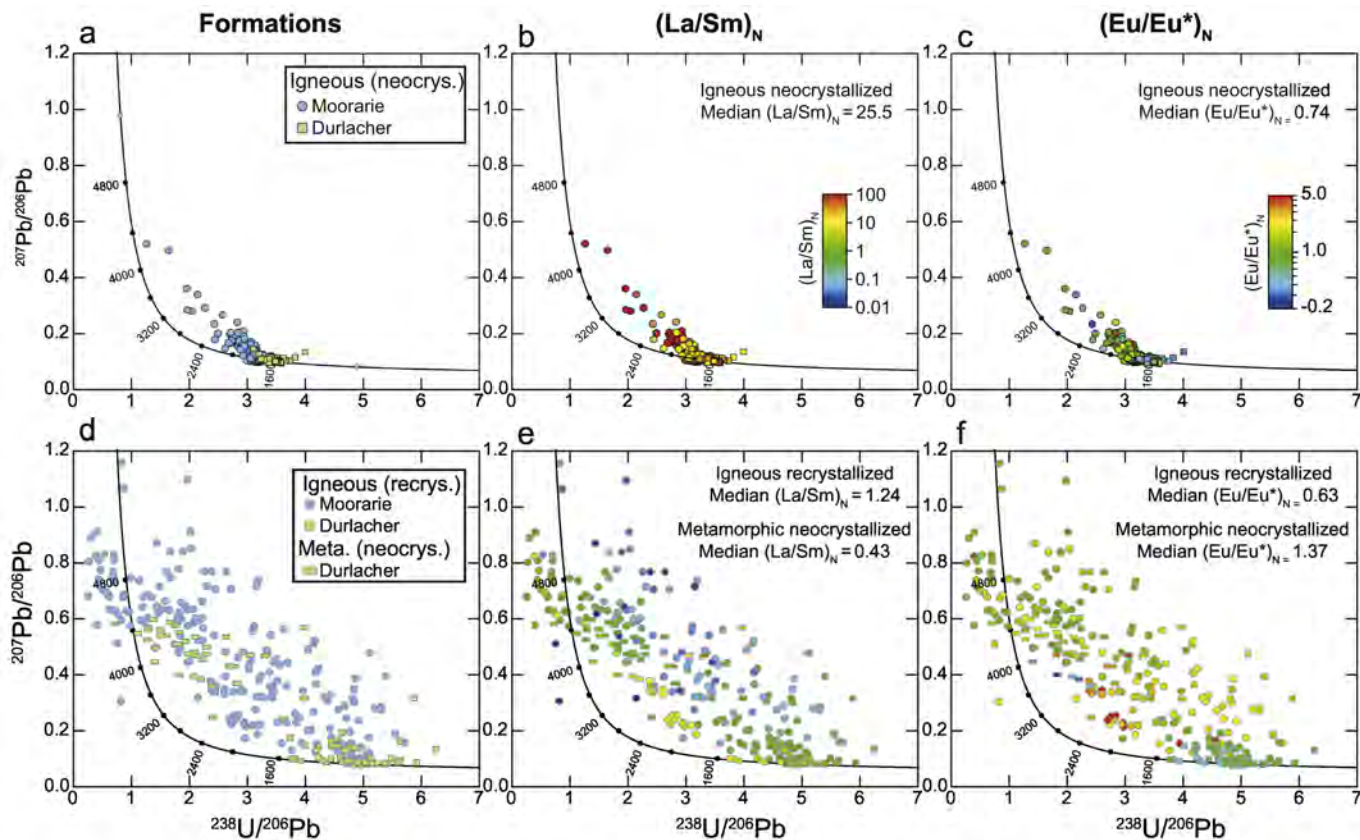


Figure 8

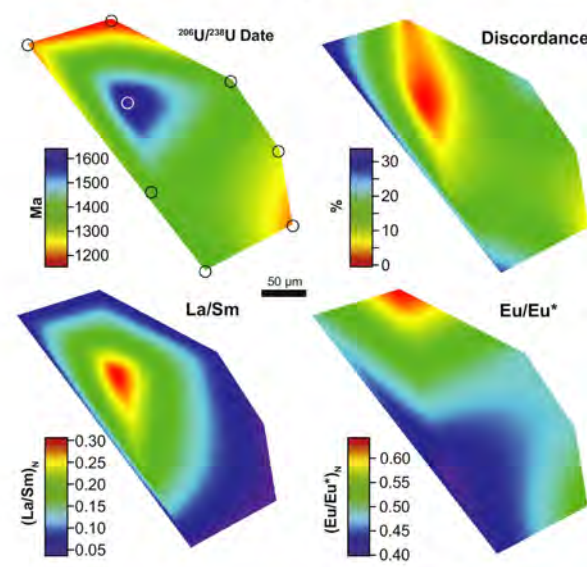
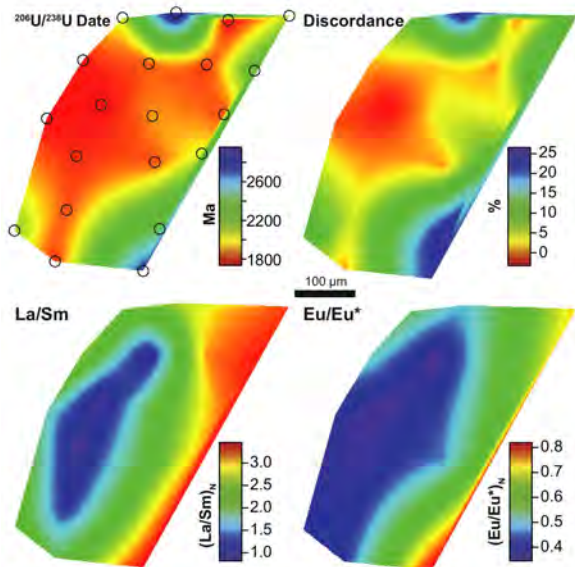
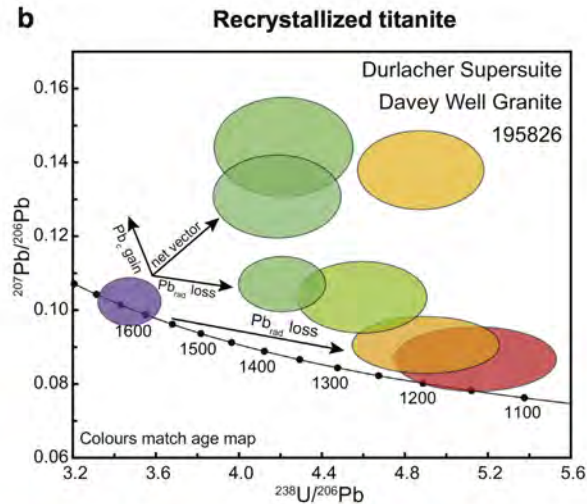
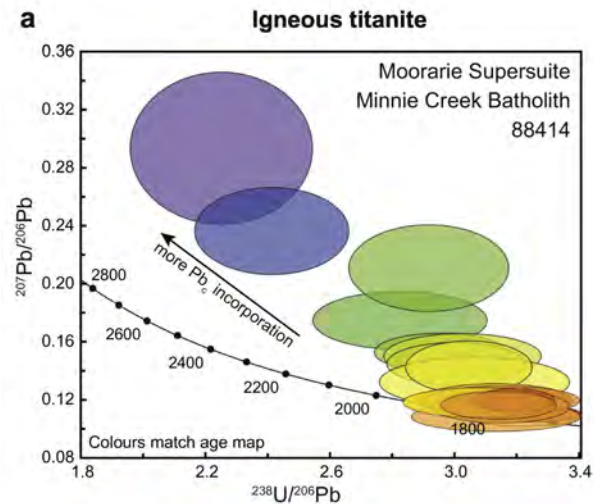


Figure 9

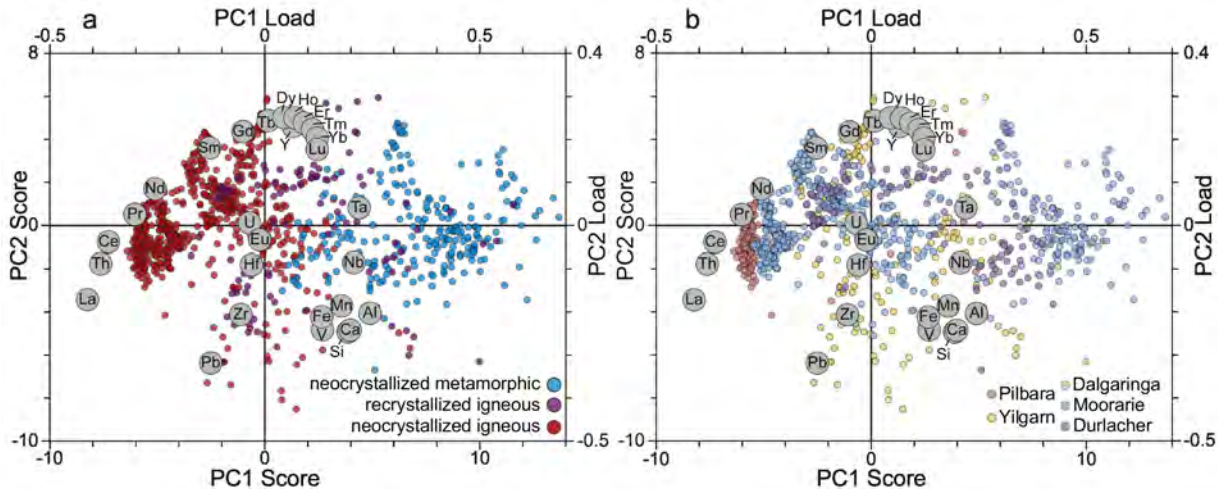


Figure 10

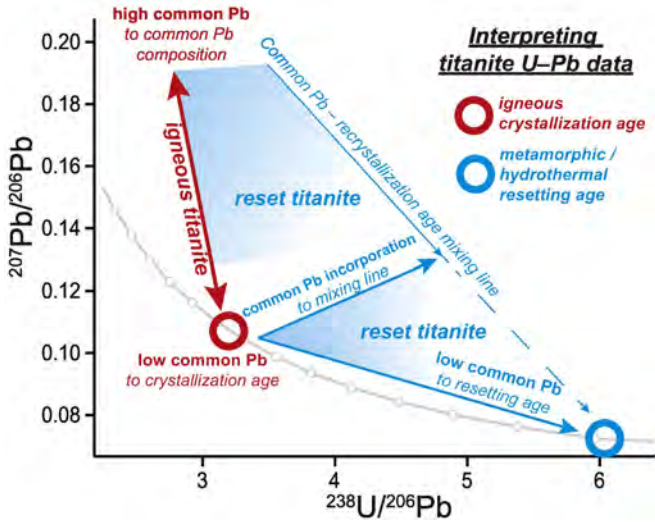


Figure 11

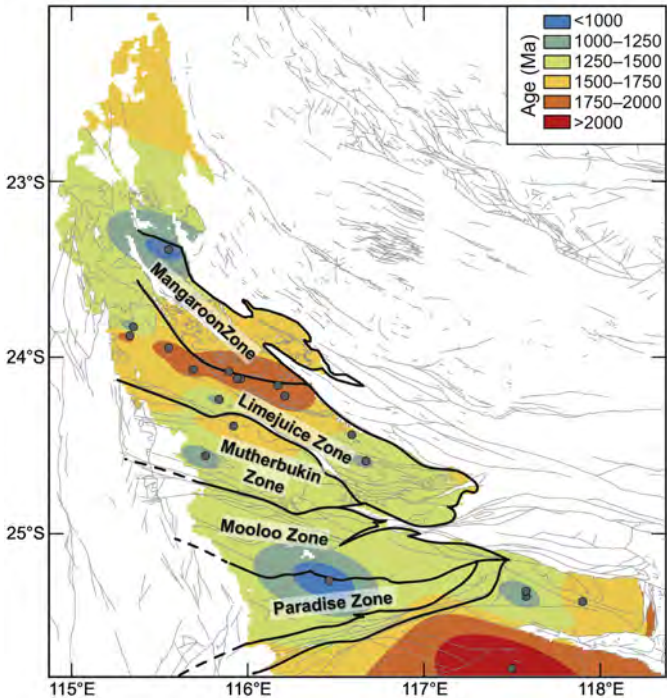


Figure 12